



Palaeoshoreline reconstruction and underwater archaeological potential of Liman Tepe: A long-occupied coastal prehistoric settlement in western Anatolia, Turkey

Nicholas L. Riddick ^{a, **}, Joseph I. Boyce ^{a, *}, Gillian M. Krezoski ^b, Vasıf Şahoğlu ^c, Hayat Erkanal ^c, İrfan Tuğcu ^d, Yeşim Alkan ^d, Jeremy J. Gabriel ^a, Eduard G. Reinhardt ^a, Beverly N. Goodman-Tchernov ^e

^a School of Earth, Environment and Society, McMaster University, 1280, Main St. W., Hamilton, ON, L8S 4K1, Canada

^b Department of Geography, University of Victoria, Victoria, Canada

^c Department of Archaeology, Ankara University, Ankara, Turkey

^d Department of Archaeology, Osmaniye Korkut Ata University, Osmaniye, Turkey

^e Department of Marine Geosciences, University of Haifa, Haifa, Israel

ARTICLE INFO

Article history:

Received 5 August 2021

Received in revised form

16 November 2021

Accepted 21 November 2021

Available online 8 December 2021

Handling Editor: Dr I Hendy

Keywords:

Liman Tepe

Prehistoric coastal palaeogeography

Palaeoshorelines

Relict river channels

Submerged landscapes

Underwater archaeological potential

ABSTRACT

Rising post-glacial sea levels had a major influence on the prehistoric settlement of the Aegean coastal zone. At Liman Tepe, an important Chalcolithic–Bronze Age coastal settlement on the south coast of the Bay of Izmir, archaeological evidence suggests a Neolithic (ca. 9600–5500 BCE) presence, but no settlement has been discovered on land. Sea levels during the Neolithic period were between 6 and >20 m below present and there is high potential for discovery of submerged prehistoric sites. Marine sediment coring and geophysical investigations (bathymetry, sub-bottom seismic profiling; >600 line-km) were conducted over a 4-km² inshore area to assess the underwater archaeological potential. Multi-proxy sediment analysis (sedimentary facies, micropalaeontology, micro-XRF geochemistry) was conducted on 20 cores to reconstruct the relative sea level (RSL) history and coastal palaeogeography. Palaeoshoreline positions were estimated by back-stripping of the decompacted sediment thickness from a digital bathymetric model (DBM).

The DBM reveals a drowned middle Holocene coastal plain with well-preserved relict river channels, palaeoshorelines and coastal headlands. The inshore stratigraphy consists of shoreface, foreshore and lagoonal deposits overlying terrestrial clay and palaeosols, defining a marine transgressive surface (MTS). The MTS records the inundation of the coastal plain prior to ca. 4000 BCE (transgressive systems tract; TST) and is marked in cores by an increasing abundance of foraminifera and a rise in Ca/Ti. During the Early Neolithic (ca. 6700 BCE), the shoreline was >500 m seaward (RSL ~ –14 to –16 m) and Karantina Island was a broad coastal headland with a sheltered western embayment. By the Middle Chalcolithic (ca. 4800 BCE), the coastline had transgressed ~800 m inland of the present shoreline and the Liman Tepe headland was separated from the mainland by a shallow coastal wetland. The maximum transgression (~1 km inland at ca. 4000 BCE) was followed by a shift to a high-stand systems tract (HST) and rapid coastline progradation by barrier accretion and lagoon development. Palaeogeographic maps identify areas with high underwater archaeological potential: 1) palaeoriver channels and lowland riverine habitats formed during the TST, prior to 4000 BCE, 2) submerged palaeoshorelines and coastal promontories (water depths 10–14 mbsl) with high potential for Neolithic sites, and 3) protected coastal embayments and lagoons representing possible prehistoric anchorage sites.

© 2021 Elsevier Ltd. All rights reserved.

* Corresponding author.

** Corresponding author.

E-mail addresses: nriddick@brocku.ca (N.L. Riddick), boycej@mcmaster.ca (J.I. Boyce).

1. Introduction

Global sea level rise since the last glacial maximum (LGM; ca. 30–20 ka BP) dramatically altered coastlines worldwide and was an

important influence on prehistoric settlement in coastal areas (Bailey and Flemming, 2008; Flatman and Evans, 2014; Flemming et al., 2017; Sakellariou and Galanidou, 2017). It has been estimated that worldwide, more than 20 million km² of coastal landscapes were inundated as postglacial sea levels recovered from the LGM maximum lowstand (~120–135 m below present) (Clark et al., 2009; Bailey et al., 2017). These drowned landscapes were former terrestrial and coastal habitats available for prehistoric human migration, settlement, and the procurement of marine resources (Bailey and Flemming, 2008; Harff et al., 2016; Benjamin et al., 2017). The archaeological potential of drowned landscapes is now widely recognized, and they have become a major focus of underwater archaeological and geoarchaeological research (Flatman and Evans, 2014; Flemming et al., 2017; Bailey et al., 2020; Flemming, 2020).

In the Aegean, sea-level rise was an important determinant on the location of prehistoric coastal settlements and harbouring sites (Harff et al., 2016; Benjamin et al., 2017). During the early postglacial, sea levels rose rapidly until ca. 6–7 ka BP, when ice volumes stabilized, and sea-level rise decelerated (Lambeck, 1995). Glacio-hydro-isostatic adjustment, between 6 and 2 ka BP, resulted in a further 4–5 m of relative sea level rise. Due to the complex geological and tectonic setting of the Aegean, sites in close geographic proximity may have significantly different tectonic and relative sea level (RSL) histories (Vacchi et al., 2014). For example, the well-studied coastal archaeological sites at Kenchreai and Lechaion in Greece, located ~10 km apart, have undergone relative subsidence and uplift, respectively (Rothaus et al., 2008; Morhange et al., 2012; Stiros, 2020; Riddick et al., 2021a). The prediction of shoreline positions is further complicated because local RSL records often differ significantly from global eustatic and regional glacio-hydro-isostatic models for the Aegean (Lambeck, 1995; Vacchi et al., 2014). Consequently, the modern shoreline position and coastal geomorphology are often poor predictors of prehistoric coastal palaeogeography and the location of settlements and harbour sites (Tartaron et al., 2011; Tartaron, 2013). The reconstruction of palaeocoastlines requires a detailed understanding of changes in RSL and the use of multi-proxy geoarchaeological techniques to determine past changes in coastal environments (Bailey and Flemming, 2008; Micallef et al., 2013; Beck et al., 2021; Aucelli et al., 2021).

In this study, we employed marine coring and geophysical surveys to investigate the underwater archaeological potential of Liman Tepe (prehistoric Clazomenae), a long-occupied coastal prehistoric settlement in western Anatolia, Turkey (Fig. 1a). Liman Tepe was an important maritime trade centre during the Early Bronze Age (EBA; ca. 3000–2000 BCE) as part of the Anatolian Trade Network (Şahoğlu, 2005). The EBA citadel of Liman Tepe was located on small coastal headland overlooking the Bay of Izmir and was protected by bastioned fortification walls (Erkanal, 2008; Tuncel and Şahoğlu, 2018). Land excavations at Liman Tepe have uncovered evidence for Chalcolithic (ca. 5600–3000 BCE) settlement and pottery evidence for a Neolithic occupation (ca. 9600–5600 BCE) (Erkanal, 2008). To date, however, no Neolithic settlement has been discovered at Liman Tepe or its environs. Neolithic settlements are known from Izmir (60 km to the west; Fig. 1a) and in the surrounding region, indicating the broad potential for sites of this age in the Bay of Izmir (Koparal et al., 2018).

The absence of Neolithic settlement layers at Liman Tepe may indicate a lack of settlement on the headland (Fig. 1b) but does not rule out the potential for submerged prehistoric sites, as significant changes in RSL and shoreline positions have occurred during the Holocene (Goodman et al., 2008). The Bay of Izmir has a relatively shallow water depth (maximum ~90 m) and was an emergent coastal plain with river valleys during the LGM (Fig. 1a). Due to its

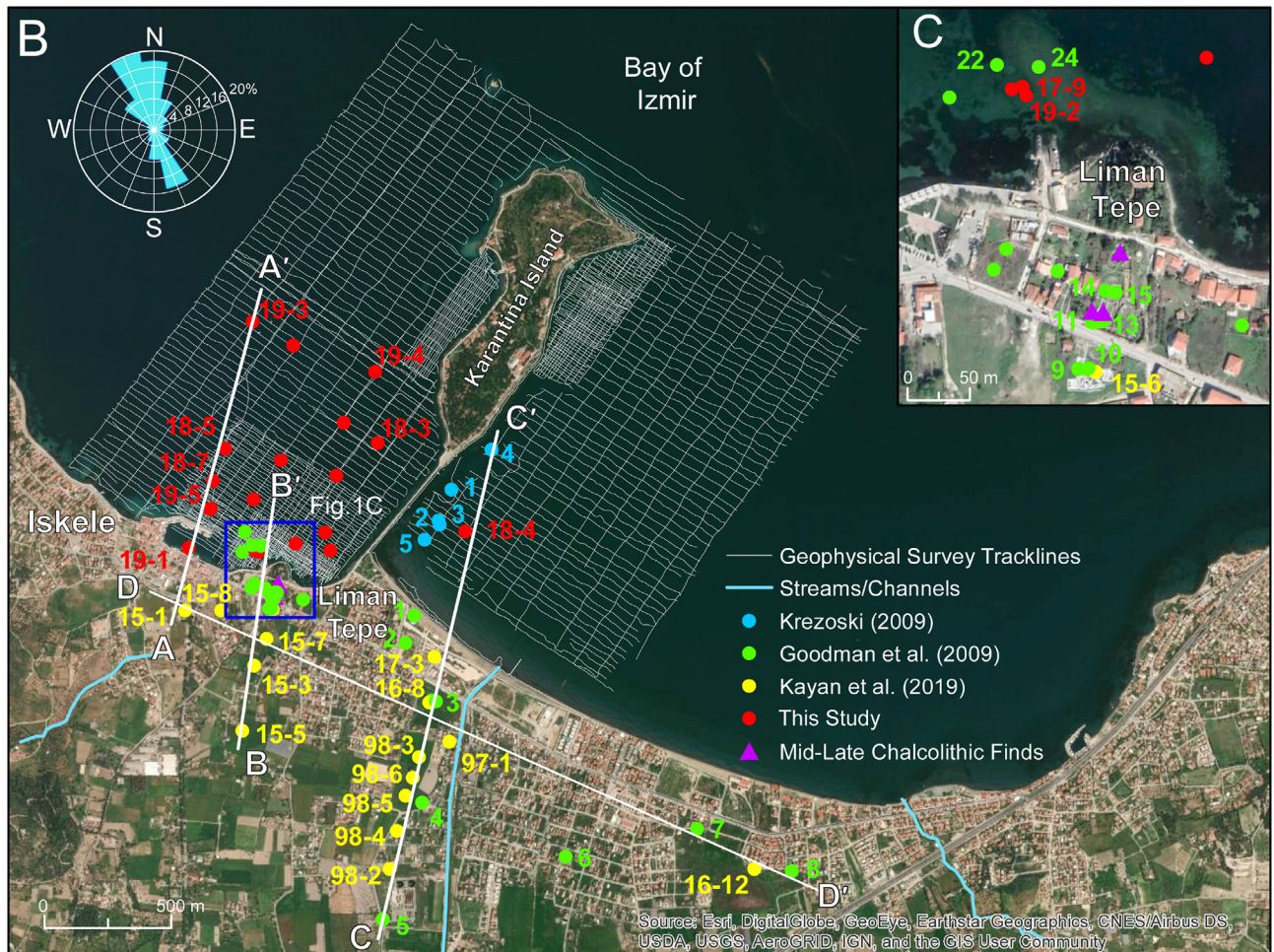
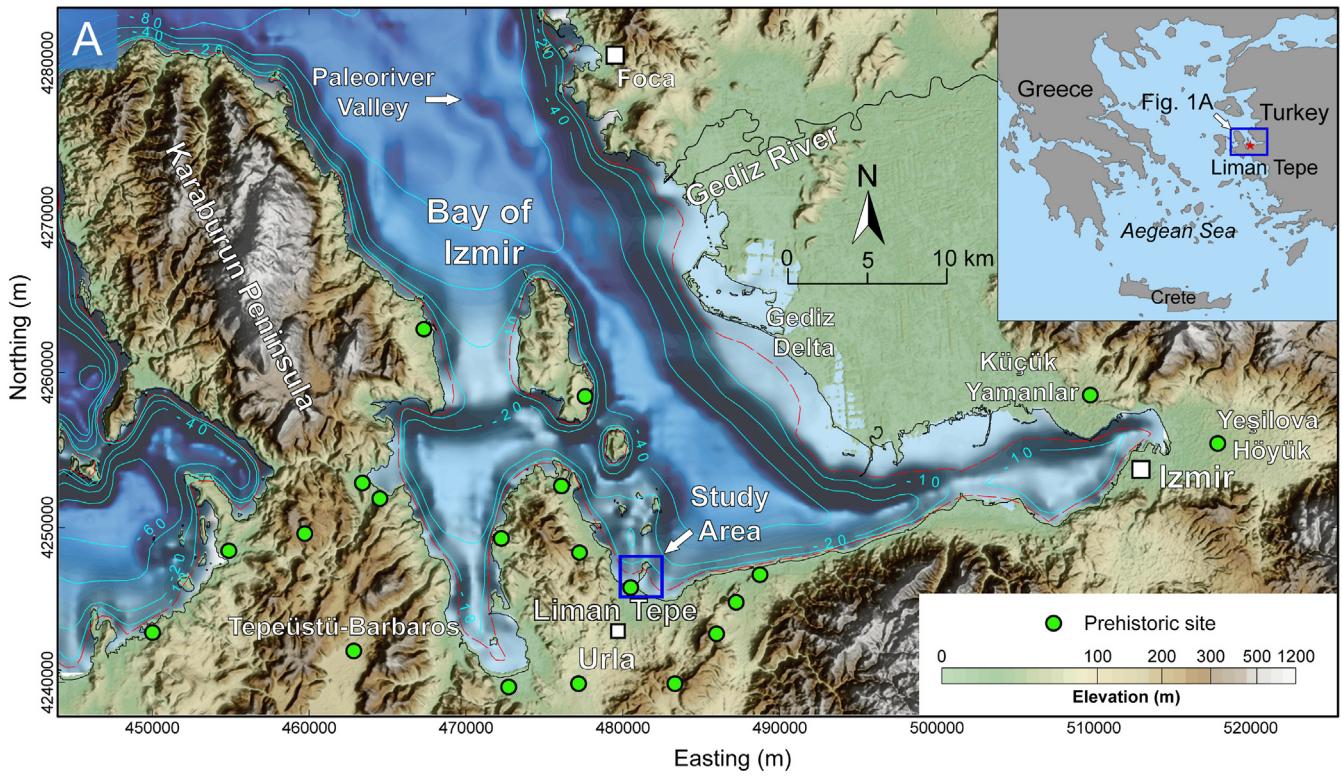
low surface gradient, the former coastal plain was rapidly inundated by rising post-glacial sea levels until ca. 4000 BCE, when global ice volumes stabilized, and the rate of sea-level rise decelerated (Lambeck, 1995; Lambeck et al., 2014). During this period, most eastern Mediterranean clastic coastlines regressed and river deltas built seaward as the sediment supply on coasts outpaced the reduced rate of sea-level rise (Anthony et al., 2014; Giaime et al., 2019). At Liman Tepe, the middle Holocene phase of rapid sea-level rise is recorded by submerged river channels and palaeoshorelines discovered in bathymetric mapping of the inshore area (Boyce et al., 2007; Krezoski, 2008). The river palaeochannels extend >300 m offshore (Figs. 2 and 3) where they terminate at a break in slope that represents a palaeoshoreline (Krezoski, 2008). The age of the palaeoshoreline was not determined due to a lack of offshore core data and radiocarbon dates. The aim of this study was to investigate submerged landscape features using marine coring and geophysical surveys and to reconstruct the Neolithic to EBA (ca. 6700–3000 BCE) coastal palaeogeography and environments. The new palaeogeographic maps identify several areas with high underwater archaeological potential, including submerged promontories, river palaeochannels, and sheltered embayments that would have been favourable locations for prehistoric settlement, resource procurement and harbouring. The maps provide important baseline data that will guide future underwater exploration for prehistoric sites in the south Bay of Izmir (Fig. 1a). The palaeoshoreline reconstruction methods reported here can also be applied more broadly in the exploration of drowned landscapes in the Aegean and in other shallow shelf environments.

2. Study area

2.1. Physical setting and geology

Liman Tepe is located near Urla on the south shore of the Bay of Izmir, in western Anatolia, Turkey (Fig. 1a). The Bay of Izmir is a microtidal bay with semi-diurnal tides (~20–50 cm) and a maximum water depth of about 90 m (Fig. 1a). Within the study area (4 km²) water depths are generally <25 m within 1 km of the shoreline (Figs. 1b and 2). Water circulation patterns in the bay are controlled by wind, thermohaline mixing, and water interchange with the Aegean Sea (Sayın, 2003). The prevailing winds during most of the year are from the north-northwest (Çoşkun and Balas, 2018) (Fig. 1b) and in the eastern Bay of Izmir, wind-driven surface currents flow clockwise, generating westerly longshore transport along the south shore, from Izmir towards Urla (Sayın, 2003; Sayın and Eronat, 2018). The primary sediment and freshwater inputs are from the Gediz River, on the north shore of the Bay of Izmir (Fig. 1a) (Duman et al., 2004). Due to the westward longshore transport along the south coast, sediment accumulation is greatest on the eastern side of Karantina Island (Figs. 1b and 2a). Coastal progradation here has been accelerated by a causeway linking the island to the mainland (Goodman et al., 2008; Krezoski, 2008). The barrier was constructed by the forces of Alexander the Great (4th c. BCE) and has undergone several phases of renovation and reconstruction (Heisserer, 1980; Krezoski, 2008). Due to the restriction of longshore flow by the causeway, beaches to the west of the barrier are sediment starved, and prone to coastal erosion. This is evident in the presence of submerged landscape features to the west of Karantina Island, which would otherwise have been buried by longshore sediment transport and shoreline progradation (Figs. 1b, 2 and 3).

The Bay of Izmir lies at the western end of the Gediz Graben, in the Aegean Extensional Province of western Turkey (Bozkurt and Sozibilir, 2004; Çiftçi and Bozkurt, 2009; Jolivet et al., 2013). Extension has been ongoing since the late Oligocene–Early Miocene



and is associated with active tectonism and destructive earthquakes (Taymaz et al., 2007; Tan et al., 2008). The bedrock in the Urla region comprises Neogene clastic and carbonate sediments, which are intercalated with Middle-Late Miocene calc-alkaline volcanic rocks (Agostini et al., 2010). The Liman Tepe headland is formed from Neogene limestones and mudstones (Urla Limestone) (Kayan et al., 2019). The bedrock surface is overlain by a variable thickness of Quaternary alluvial and coastal plain sediments (Aksu et al., 1987; Duman et al., 2004; Goodman et al., 2009). Within the study area, Quaternary sediments are between 1 and 18 m thick (Kayan et al., 2019). The modern beach and foreshore deposits consist of clastic sediments with a variable component of biogenic (e.g. mollusk shell fragments) and detrital carbonate clasts (Duman et al., 2004). Shoreface sediments are dominantly silt and mud with abundant marine organic matter. *Posidonia oceanica* seagrass is the primary component of marine plant organics in sediments and forms extensive meadows in the shallow inshore areas (~2–35 m water depth) (Dural et al., 2012; Votruba et al., 2016).

3. Methods

3.1. Geophysical surveys

Bathymetric and sub-bottom seismic surveys were conducted across a 4-km² area around Liman Tepe and Karantina Island (>600-line km; Fig. 1b) using a Knudsen 320BP echosounder system. Single-beam bathymetry (200 kHz) and high-frequency (18–24 kHz) seismic profiles were acquired at 5–75 m line spacings (Fig. 1b) and survey navigation recorded by an onboard differential GPS with sub-metre positioning accuracy. Bathymetric data processing included application of time-varying gain and corrections for tides and sensor heave (Sonnenburg and Boyce, 2008). Bathymetry data were gridded using a triangular irregular network (TIN) interpolation to produce a digital bathymetric model (DBM) (Fig. 2). Seismic processing included automatic gain control (AGC), band-pass filtering (10–20 kHz) and depth-conversion of two-way travel times using an estimated p-wave velocity of 1550 ms⁻¹ for marine sediments.

3.2. Coring and sediment analysis

Twenty sediment cores (2–5 m length) were collected in water depths of up to 15 m using a percussion coring system with 75-mm-diameter aluminum tubes (Riddick, 2021) (Figs. 1b, c). Cores were extracted using a boat-mounted winch system, sealed and refrigerated (4–6 °C) to limit sediment oxidation and bacterial growth prior to analysis. Cores were split and one half sampled for micropalaeontological analysis, and an archive half retained for micro-XRF core scanning (μ -XRF-CS). Core compaction was determined as the ratio of recovered core length to core tube penetration and a linear decompaction correction was applied to all cores (Morton and White, 1997). Core compaction (5–47%) was greatest in long cores containing thick sections of organic-rich muds. Core sedimentary lithofacies and texture were described and logged in detail, and genetically-related facies grouped into lithofacies assemblages (Dalrymple and James, 2010). Petrographic analysis was conducted on eight volcanic bedrock and beachrock samples using polarized light microscopy to determine modal compositions.

Marine core data were combined with borehole data from three previous studies (Goodman et al., 2008, 2009; Krezoski, 2008;

Kayan et al., 2019) to correlate and interpret the offshore and onshore stratigraphy. The assembled core database includes >40 boreholes and is one of the largest assembled in the geo-archaeological study of a prehistoric coastal archaeological site in the Aegean (Fig. 1b).

3.3. Micropalaeontology

For micropalaeontological analysis, 2.5 cc sediment samples were collected above and below major lithologic contacts in four cores (18-5, 19-1, 19-3, 19-4; Fig. 1b) to document the terrestrial-wetland to marine transition. Samples were divided into eight aliquots using a settling tube and foraminifera separated using wet sieving methods (Scott and Hermelin, 1993). Foraminifera counts were made to ~100 individuals and identified to the *genus* level to determine presence/absence of foraminifera at key lithostratigraphic boundaries. Identification was assisted by two previous studies, which had identified foraminifera to the species level (Goodman, 2006; Krezoski, 2008).

3.4. Micro-XRF geochemistry

Micro-XRF elemental analysis was conducted on nine marine cores to assist in identification of the marine-terrestrial transition. Split cores were analyzed at 500 μ m intervals on an Itrax core scanner (Cox Analytical Systems) using a Mo tube with 30 kV/25 mA power settings and a 20s exposure time (Löwemark et al., 2011). Element values were normalized to the ratio of coherent/incoherent back scatter to minimize matrix effects produced by downcore changes in sediment porosity, water content and grain size (Gregory et al., 2019). The Ca/Ti ratio was selected from the available elements as an indicator of the relative influence of marine versus terrigenous inputs to the basin and used to correlate the marine-terrestrial transition (Piva et al., 2008; Ingram et al., 2010; Tjallingii et al., 2010; Koster et al., 2015; Pint et al., 2015; Rothwell and Croudace, 2015).

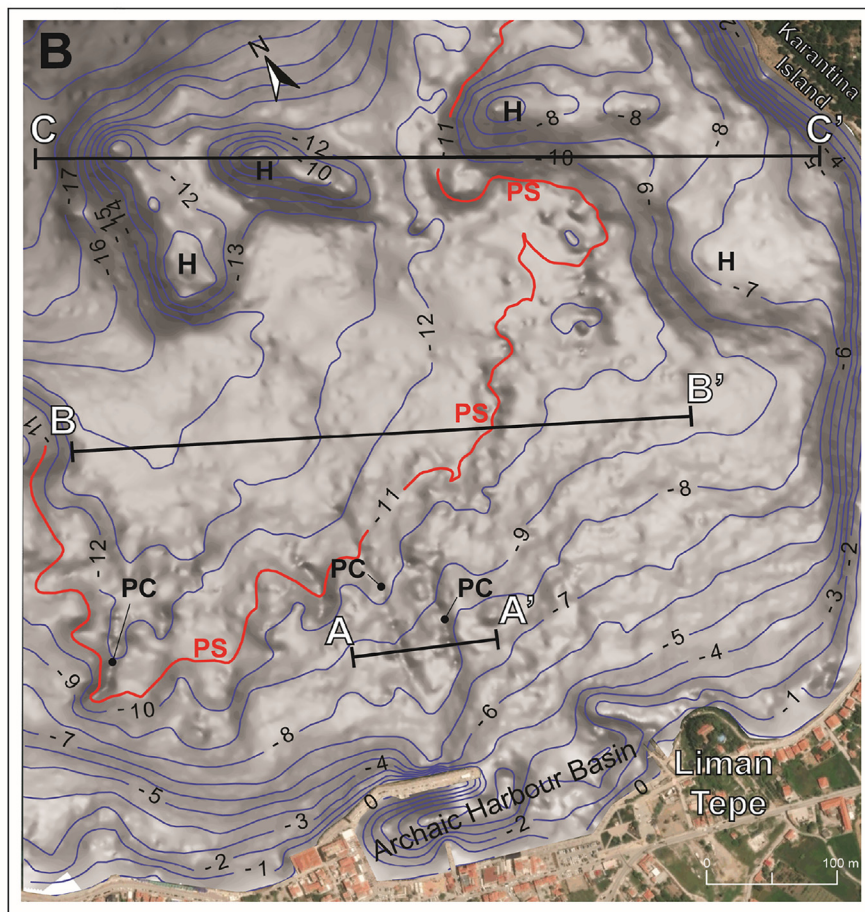
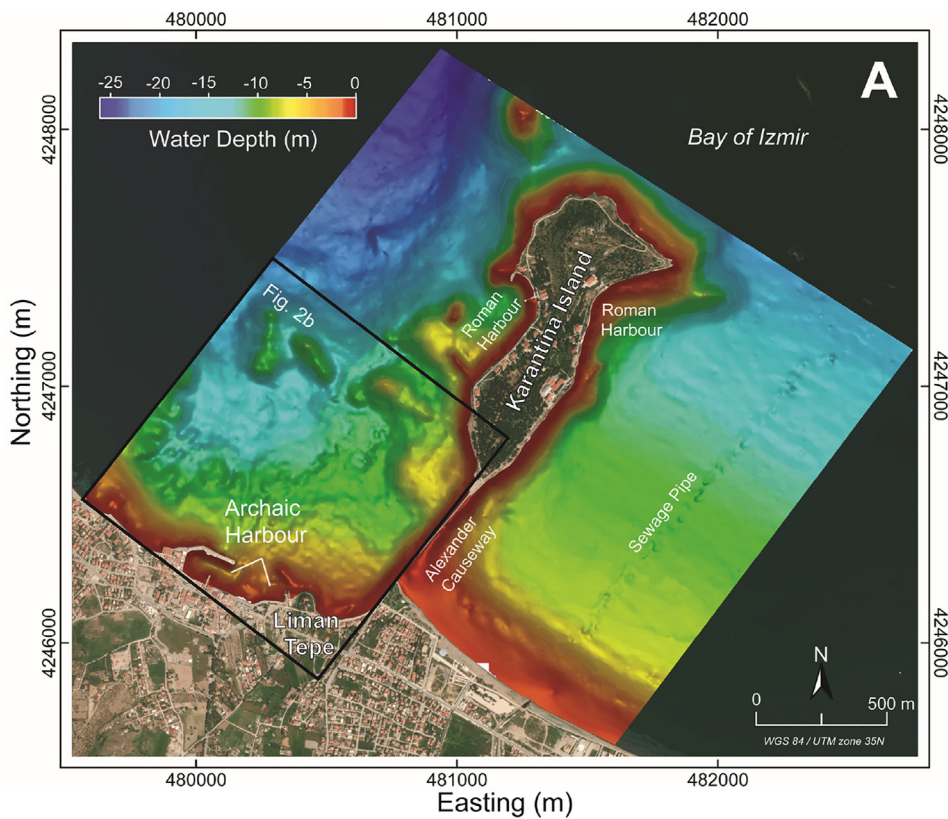
3.5. AMS ¹⁴C chronology

AMS ¹⁴C dating was conducted on 31 organic samples (A.E. Lalonde AMS Laboratory, University of Ottawa) from 9 cores and combined with 14 dates available from previous studies (Goodman, 2006; Krezoski, 2008) (Table 1). Conventional radiocarbon ages were calibrated using Calib 8.2 (Stuiver et al., 2020) with the IntCal20 and Marine20 calibration curves (Reimer et al., 2020; Heaton et al., 2020). A marine reservoir correction was applied to shell and marine plant organic samples using a mean $\Delta R = -26 \pm 67$, calculated on three Aegean values in the Calib 8.2 Marine20 online database (Reimer and McCormac, 2002; Heaton et al., 2020). Age constraints were also provided by ages obtained on ceramics and other diagnostic cultural materials in sediments. Bayesian sediment age-depth models were constructed for five cores (17-9, 18-3, 18-5, 19-1, and 19-4; Fig. 1b) using *rBACON* (v. 2.5.6; Blaauw and Christen, 2011).

3.6. RSL and palaeoshoreline reconstructions

Palaeoshoreline positions were estimated using a modification of the sediment back-stripping approach described by Sonnenburg et al. (2012). Back-stripping techniques are employed increasingly

Fig. 1. A. Digital elevation model and generalized bathymetry of the Bay of Izmir (derived from SRTM30_PLUS data; Becker et al., 2009) with location of Liman Tepe and other prehistoric land archaeological sites (modified from Koparal et al., 2018). Location in western Anatolia shown in inset. B. Study area map showing core locations, stratigraphic profiles (Figs. 8 and 9) and geophysical survey track lines (>600 line-km). Wind rose shows dominant wind directions at Urla Meteorological Station (modified from Coşkun and Balas, 2018). C. Liman Tepe archaeological site showing locations of marine and land cores.



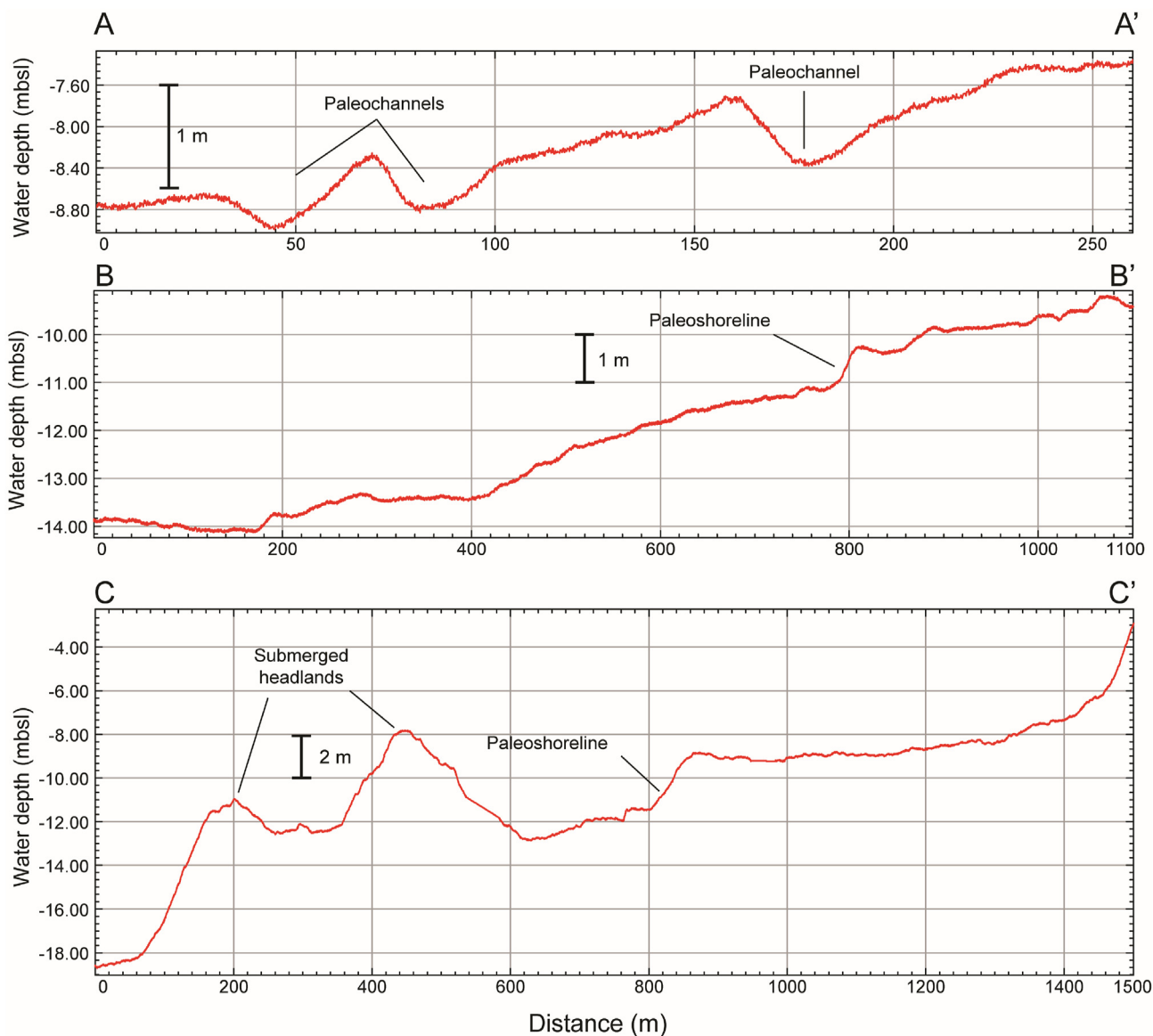


Fig. 3. Bathymetric profiles showing submerged landscape features. Profile locations in Fig. 2b. A. Submerged palaeochannels recording a submerged coastal plain and river system at -8 to -9 mbsl. B. Low-relief (~1.5-3 m) scarp indicating a palaeoshoreline feature. C. Submerged promontories and paleoshoreline on western side of Karantina Island. The promontories and river floodplain were sub-aerially exposed during the mid-Holocene (ca. 6700 BCE) when sea levels were >16 m below present sea level.

in coastal palaeogeographic reconstructions, as they can yield improved estimates of shoreline positions when compared with models using the modern seabed bathymetry (Westley et al., 2014; Conolly and Obie, 2021). As a first step, a revised RSL curve was constructed by combining sea level indicators from two previous studies (Goodman et al., 2008; Krezoski, 2008) with 10 new RSL markers from marine sediment cores. RSL marker elevations were corrected for post-depositional lowering due to autocompaction (Allen, 2000; Brain et al., 2015) using the 1-D geotechnical model of Paul and Barras (1998). The elevations of the marine transgressive surface (MTS) identified in marine and land cores in previous studies (Goodman et al., 2008, 2009; Kayan et al., 2019) were also

corrected for autocompaction, using the reported sediment texture to estimate the liquid limit (i.e., 25% for lean silty sands and 75% for plastic clays) (Paul and Barras, 1998). Autocompaction corrections ranged from 0.1- 1.2 m and were greatest for long cores containing thick sections of mud and silt facies. An isochore map of the sediment thickness above the MTS was constructed using the compaction-corrected values and back-stripped (subtracted) from the DBM (Fig. 2). The back-stripped bathymetric surface represents the estimated elevation of the MTS relative to modern sea level. In a final step, palaeoshoreline positions were estimated by projecting the estimated RSL elevations at several time steps (6700-4000 BCE) onto the MTS and plotted as an overlay on the DBM.

Fig. 2. A. Colour-shaded digital bathymetric model (DBM) for ~4-km² inshore area at Liman Tepe. Note smooth, low-relief seabed to east of Karantina Island due to westward longshore sediment transport and shoreline progradation on eastern side of the Alexander causeway. The linear feature in bathymetry to east of Karantina Island is a sewage pipe trench. B. Grey-shaded bathymetric map (~1 km²) showing submerged palaeolandscapes on the west side of Karantina Island: PC = palaeochannels, PS = palaeoshoreline, H = submerged headlands. Locations of bathymetric profiles (Fig. 3) indicated. (For interpretation of the references to colour in this figure legend, the reader is referred to the Web version of this article.)

Table 1

AMS ^{14}C radiocarbon dates. All dates calibrated with Calib 8.2 (Stuiver et al., 2020) using the IntCal20 and Marine20 calibration curves (Reimer et al., 2020; Heaton et al., 2020). Dates from Goodman (2006; G4-23) and Krezoski (2009; K1–K4) also re-calibrated. *Marine reservoir correction $\Delta R = -26 \pm 67$ applied using three Aegean values from Reimer and McCormac (2002) in the Marine20 online database (<http://calib.org/marine>). Sample elevations corrected for post-depositional compaction. ** Suess Effect.

Lab Code	Core #	Material	Elevation (m bsl)<	Corrected Elevation (m bsl)	^{14}C Age (BP)	Cal. Age BCE/CE (2σ)	Median Probability BCE/CE
Beta-194729	G-8	Peat	1.90	1.43	2770 ± 40	922-800 BCE	856 BCE
Beta-194730	G-7	Peat	3.26	2.78	4080 ± 40	2704-2553 BCE	2631 BCE
Beta-194731	G-7	Peat	1.85	1.38	2700 ± 40	922-800 BCE	856 BCE
Beta-194732	G-8	Shell*	4.35	4.27	4370 ± 40	2662-2139 BCE	2404 BCE
Beta-191877	G-4	Shell*	0.59	0.50	4370 ± 40	2662-2139 BCE	2404 BCE
Beta-191878	G-23	Shell*	7.66	7.61	3230 ± 40	1202-761 BCE	961 BCE
Beta-191879	G-23	Shell*	8.60	8.60	5420 ± 40	3922-3480 BCE	3681 BCE
Beta-191880	G-22	Shell*	7.60	7.60	6280 ± 40	4824-4372 BCE	4600 BCE
Beta-191881	G-10	Bone	1.60	1.57	3950 ± 40	2502-2338 BCE	2455 BCE
Beta-166694	G-11	Peat	2.30	1.95	4570 ± 40	3244-3102 BCE	3298 BCE
Beta-164096	G-24	Plant fragments	5.8	n/a	2710 ± 30	910-807 BCE	858 BCE
Beta-243245	K-1	Seaweed*	6.68	6.63	1810 ± 40	530-941 CE	722 CE
Beta-234186	K-4	Olive pit	5.52	5.48	2360 ± 40	545-370 BCE	446 BCE
Beta-234187	K-4	Seaweed*	6.47	6.44	5090 ± 40	3549-3047 BCE	3319 BCE
UOC-7342	17-9	Plant fragments	5.16	5.13	2960 ± 22	1261-1110 BCE	1172 BCE
UOC-9339	17-9	Plant fragments	5.54	5.51	3550 ± 25	1959-1871 BCE	1895 BCE
UOC-9340	17-9	Plant fragments	5.96	5.93	3966 ± 25	2503-2449 BCE	2489 BCE
UOC-7343	17-9	Plant fragments	6.24	6.22	4535 ± 22	3240-3103 BCE	3206 BCE
UOC-9341	17-9	Plant fragments	6.38	6.36	4682 ± 25	3474-3372 BCE	3441 BCE
UOC-7344	17-9	Plant fragments	6.51	6.50	4996 ± 22	3916-3877 BCE	3764 BCE
UOC-10196	18-3	Seaweed*	7.60	7.56	1519 ± 25	818-1220 CE	1019 CE
UOC-10197	18-3	Seaweed*	8.12	8.08	2241 ± 29	25-466 CE	253 CE
UOC-9342	18-3	Seaweed*	8.93	8.90	4518 ± 25	2853-2378 BCE	2604 BCE
UOC-9350	18-3	Shell*	9.39	n/a	7224 ± 28	5770-5406 BCE	5589 BCE
UOC-9343	18-4	Seaweed*	7.72	7.67	962 ± 25	1348-1683 CE	1519 CE
UOC-9344	18-4	Plant fragments	8.56	8.48	2123 ± 25	200-88 BCE	136 BCE
UOC-9345	18-4	Plant fragments	10.73	10.68	3180 ± 25	1501-1416 BCE	1455 BCE
UOC-9351	18-4	Shell*	11.68	11.68	4802 ± 25	3252-2729 BCE	2962 BCE
UOC-9346	18-5	Seaweed*	11.82	11.77	2322 ± 25	62 BCE-382 CE	155 CE
UOC-9347	18-5	Seaweed*	13.12	13.05	4655 ± 28	3003-2527 BCE	2766 BCE
UOC-9352	18-5	Shell*	14.78	14.71	7355 ± 25	5903-5530 BCE	5712 BCE
UOC-9353	18-5	Shell*	14.85	14.80	7523 ± 28	6058-5685 BCE	5874 BCE
UOC-12077**	19-1	Plant fragments	5.00	4.97	270 ± 23	1628-1665 CE	1640 CE
UOC-12078	19-1	Plant fragments	5.17	5.13	1330 ± 22	653-691 CE	680 CE
UOC-12824	19-1	Plant fragments	6.02	5.97	3445 ± 27	1785-1675 BCE	1755 BCE
UOC-12103	19-1	Shell*	6.52	6.47	6335 ± 25	4885-4444 BCE	4661 BCE
UOC-12825	19-1	Bulk sediment	7.03	6.91	7310 ± 43	6238-6070 BCE	6156 BCE
UOC-12220	19-1	Bulk sediment	7.17	6.98	7968 ± 35	7042-6747 BCE	6895 BCE
UOC-12079	19-2	Plant fragments	6.98	6.96	6197 ± 29	5218-5045 BCE	5131 BCE
UOC-12104	19-3	Shell*	14.93	14.74	8061 ± 27	6634-6234 BCE	6437 BCE
UOC-12080	19-4	Seaweed*	8.96	8.90	1603 ± 23	722-1123 CE	929 CE
UOC-12081	19-4	Seaweed*	11.27	11.20	4445 ± 25	2271-2257 BCE	2507 BCE
UOC-12105	19-4	Shell*	12.29	12.26	7743 ± 27	6315-5909 BCE	6104 BCE
UOC-12106	19-4	Shell*	12.49	12.48	7826 ± 28	6384-6000 BCE	6186 BCE
UOC-12107	19-5	Shell*	11.57	11.54	6284 ± 27	4822-4387 BCE	4605 BCE

4. Results

4.1. Bathymetry and seismic data

Bathymetric mapping revealed a low relief seabed topography to the west of Karantina Island and a smooth, gradually sloping seabed to the east (Fig. 2a). The smooth bottom relief in the east results from the westward longshore transport and trapping of sediment by the causeway (Goodman et al., 2008; Krezoski, 2008). In the west, the reduced sediment accumulation in the lee of barrier has limited coastal progradation and has preserved palaeoland-scape features on the submerged coastal plain, including relict river channels, palaeoshorelines, and submerged coastal promontories (Figs. 2b and 3). Palaeochannels are up to 20 m in width, 1–2.5 m in depth, and have low sinuosity, linear thalwegs (Fig. 3a). The channels extend >300 m northwest of the modern harbour breakwater where they terminate at a break in slope at –11 to –12 mbsl (metres below sea level) (Fig. 2b). The channels are infilled by up to 4 m of marine sediments, which overlie volcanic bedrock and terrestrial mud deposits (see section 4.2). The break in slope is

interpreted as a palaeoshoreline, formed during a brief sea level still-stand, or a bedrock ridge underlying the marine sediment cover. Sediment slumps visible at the base of the break in slope (Fig. 3c) indicate that the scarp has been modified by submarine mass movements (Fig. 2b). On the west side of Karantina Island, submerged promontories define a former coastal headland that enclosed an marine embayment, when sea levels were between 12 and 14 m below present (Figs. 2b and 3c).

No submerged landscape features are preserved on the seabed to the east of the causeway due to coastal progradation (Fig. 2a), but sub-bottom seismic data provide insights into the buried coastal topography and palaeogeography (Fig. 4). Seismic profiling revealed an uppermost package of acoustically transparent seismofacies overlying a continuous high-amplitude reflector at 13–15 ms (Fig. 4a). The reflector defines a basin-wide seismic horizon, marking the contact between lagoonal mud and shoreface sand facies (LA-3, LA-4) with underlying coarse gravelly deposits (Krezoski, 2008; Müller et al., 2009). The interpolated upper surface of the reflector defines a shallow basin and a broad, northwest-trending ridge (–7 to –9 mbsl) that connects the east coast of

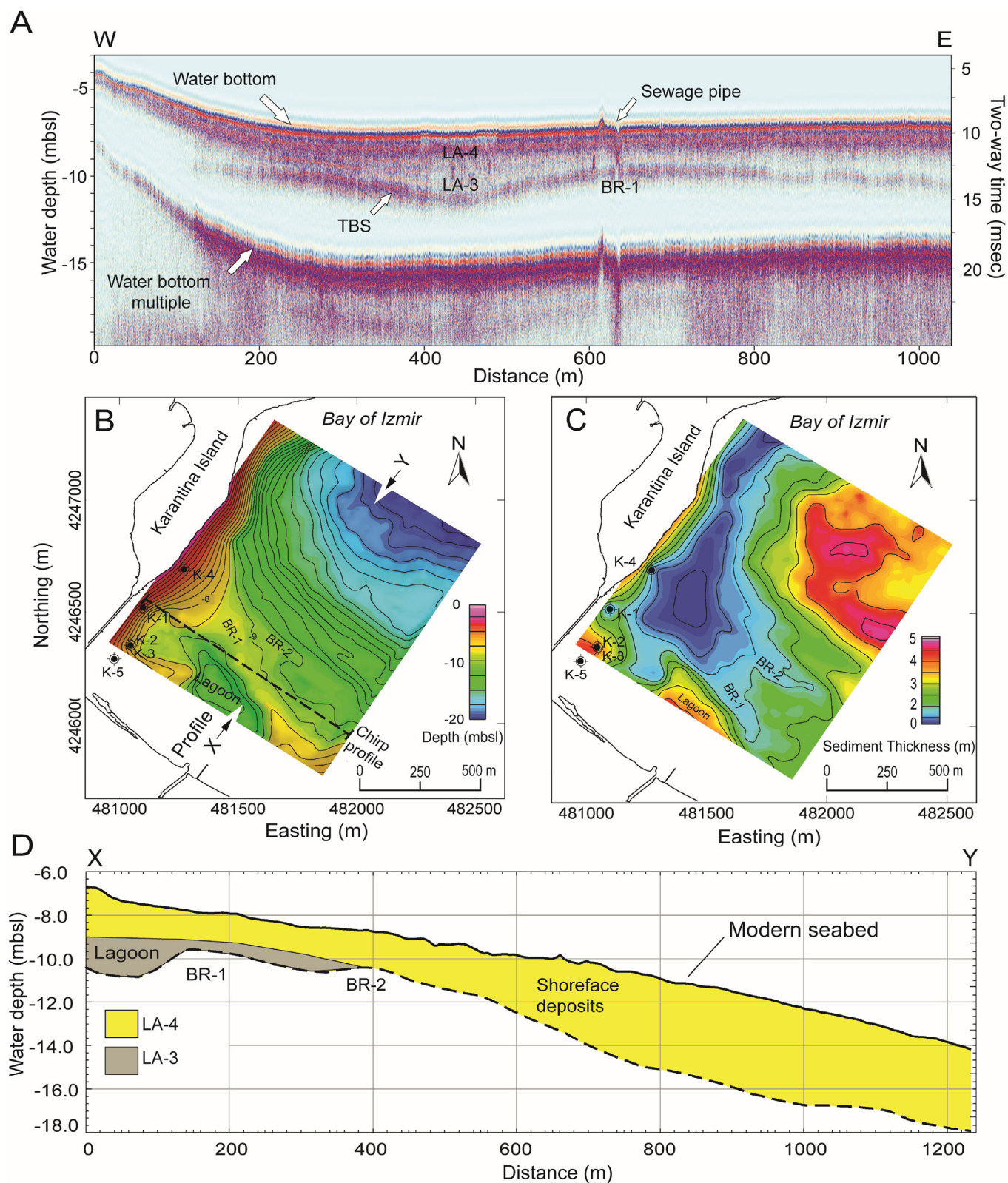


Fig. 4. A. W-E sub-bottom seismic profile (location in 4b). High-amplitude reflector at 12–15 ms records contact between foreshore sand facies and overlying shoreface silt and mud facies. High in reflector surface indicates a linear sand ridge (BR-1) interpreted as transgressive barrier system (TBS). B. Contoured upper surface of reflector defining top of shoreface deposits (contour interval 0.5 m). Northwest-southeast trending ridges are interpreted as drowned beach barriers (BR-1, BR-2). Core locations (K1-4) from Krezoski (2008). C. Isochore map (contour interval 1 m) showing thickness of LA-3/LA-4 sediments above basal reflector. Note thickening within back-barrier lagoon. D. North-south profile (X–Y; Fig. 4b) showing buried beach ridges and lagoonal deposits. Dashed line indicates seismic reflector defining top of foreshore sands.

Karantina Island with the mainland (BR-1; Fig. 4b). The 3–4 m deep basin behind the ridge is infilled with foreshore and lagoonal sediments (Fig. 4d). The ridge is interpreted as a transgressive beach barrier (BR-1; Fig. 4b), which connected Karantina Island with the mainland coast to the east (Krezoski, 2008). Other parallel beach ridges in the reflector surface (e.g. BR-2; Fig. 4d) record earlier phases of barrier-lagoon development during the middle Holocene transgression. The bedrock surface was not resolved in seismic profiles, due to the limited penetration depth of the high-frequency seismic source (Fig. 4a). However, previous low-frequency seismic profiling has recorded a total sediment thickness >8 m over bedrock to the east of the Karantina Island (Müller et al., 2009).

4.2. Holocene stratigraphy

Five distinctive lithofacies assemblages (LA 1–5) were recognized in marine cores (Figs. 5–7) and correlated with lithofacies identified in land core data (Figs. 8 and 9). The contact between lithofacies assemblages LA-2 and LA-3 represents a basin-wide parasequence boundary, marking a marine transgressive surface (MTS) that has been previously identified in land cores (Goodman

et al., 2008, 2009).

4.2.1. LA-1 (volcanic bedrock, regolith)

Bedrock was encountered at a depth of 3.8 m in a single core (19-5), comprising a thin (~20–30 cm) unit of weathered, angular volcanic rock fragments (Fig. 7c). LA-1 contained no marine fauna and was devoid of organics. The bedrock fragments were an intermediate extrusive composition (trachyte-andesite), consisting of sanidine phenocrysts set in a finer matrix of alkali feldspar, quartz, biotite, sericite, pyroxene and hornblende amphibole.

LA-1 is identified as the Middle Miocene Menteş trachyte-andesite, which forms the local bedrock to the west and south of the study area (Kaya, 1979; Göktaş, 2016). The angular shape and weathering of clasts indicates that LA-1 is a regolith (saprolite) formed by chemical weathering of volcanic bedrock.

4.2.2. LA-2 (terrestrial clays, palaeosol, alluvium)

Overlying bedrock, LA-2 was a 10–60 cm thick unit of dark grey to greenish-brown compact clay, containing abundant weathered volcanic (trachyte-andesite) clasts up to 1 cm in size and fine organic matter (Figs. 5, 6c,d and 7b). LA-2 contained no shell fragments and foraminifera were absent or in very low abundance

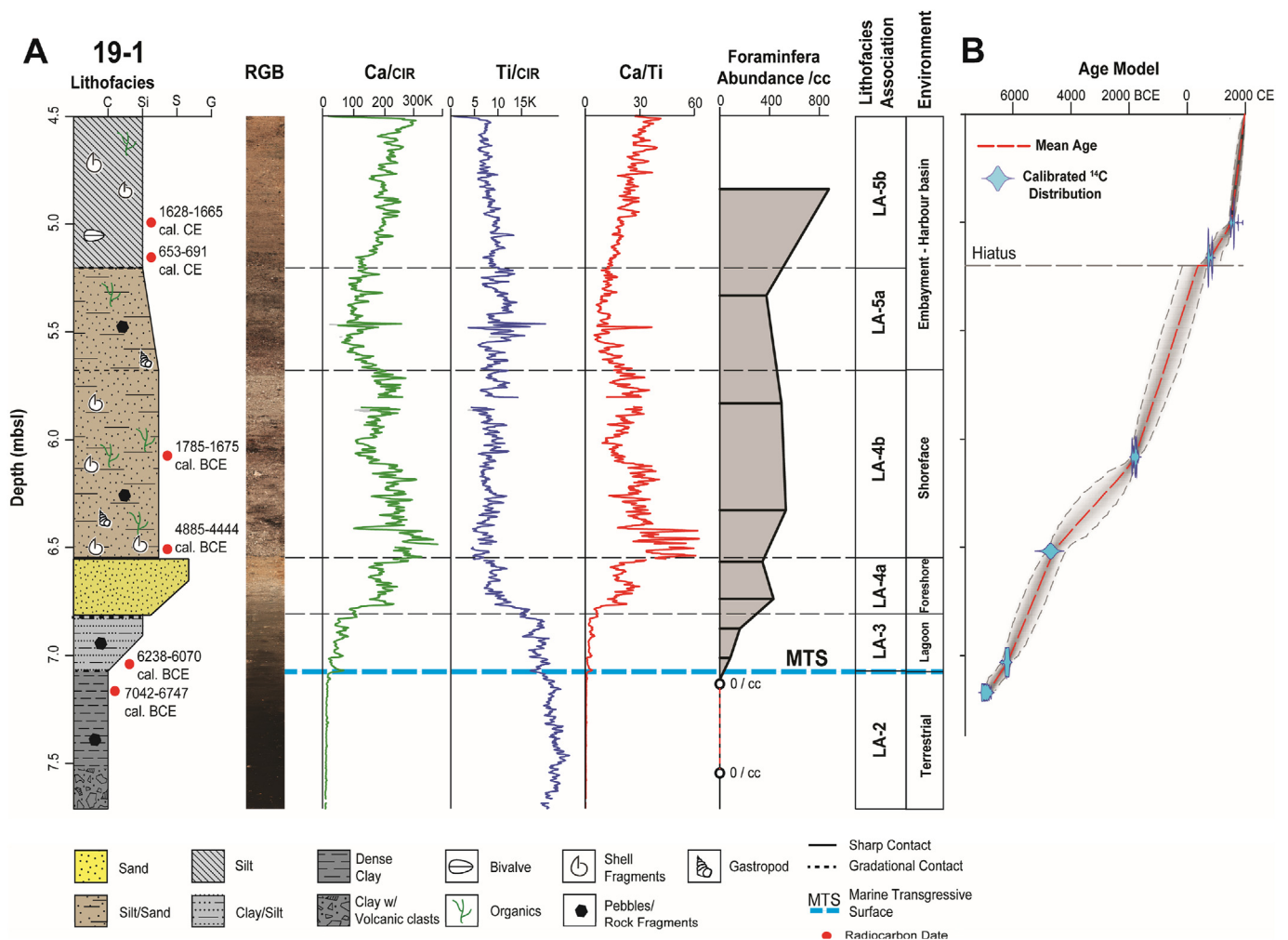


Fig. 5. A. Core 19-1 lithofacies log with AMS ¹⁴C dates, RGB scan, XRF elemental profiles and foraminifera abundance. Element profiles normalized using the ratio of coherent to incoherent scatter (CIR) to minimize matrix effects (Gregory et al., 2019). Marine transgressive surface (MTS) marked by lagoonal clay and silt facies overlying terrestrial clay deposits. Note increase in foraminifera abundance and Ca/Ti above MTS. B. Bayesian age-depth model produced in RBACON (Blaauw and Christen, 2011). Red dashed line indicates mean modelled ages and grey dashed lines, the 95% probability intervals. Calibrated distributions of individual ¹⁴C dates shown in blue. (For interpretation of the references to colour in this figure legend, the reader is referred to the Web version of this article.)

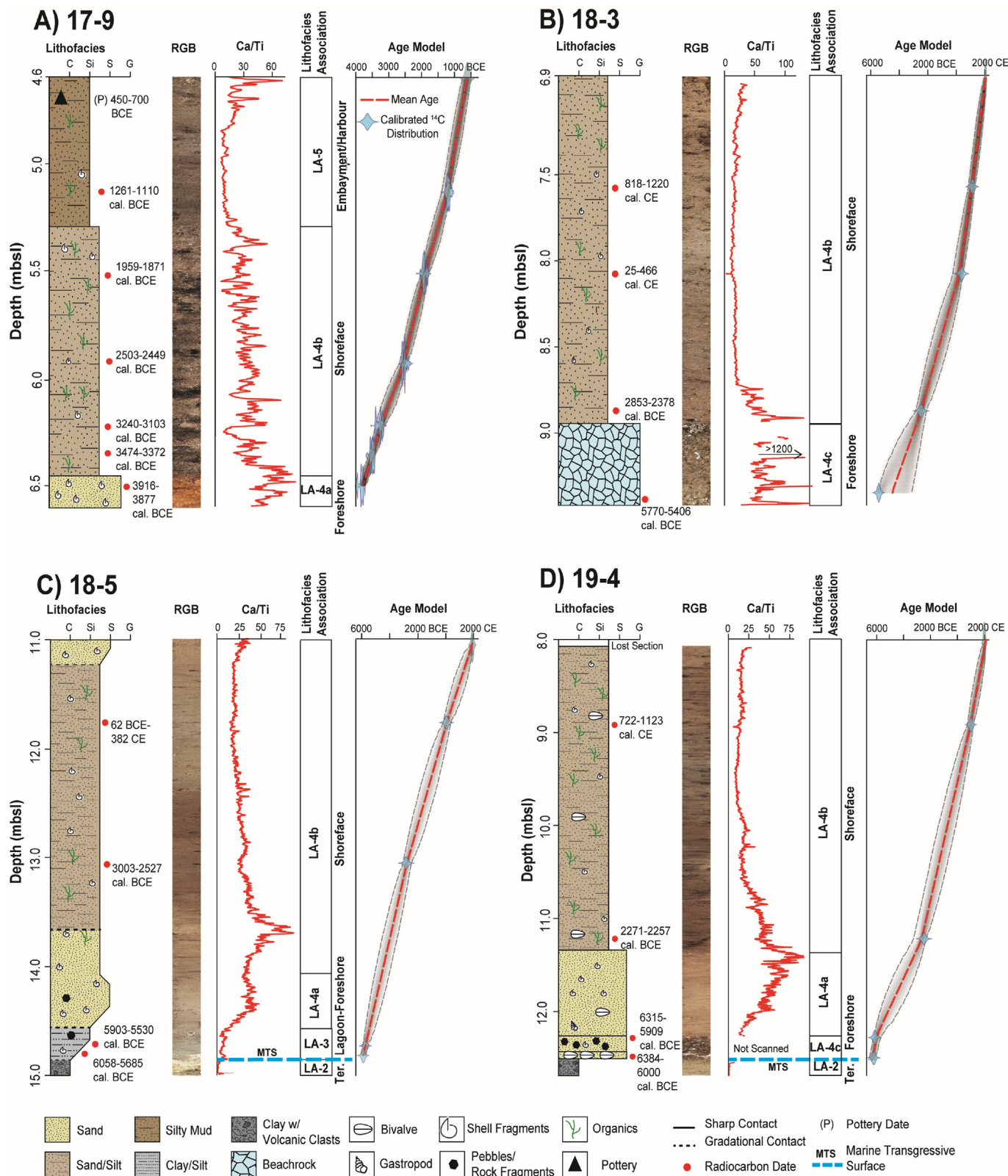


Fig. 6. Lithofacies logs, AMS ¹⁴C dates, RGB scan, Ca/Ti ratio, and Bayesian age-depth models for cores 17-9 (A), 18-3 (B), 18-5 (C), 19-4 (D).

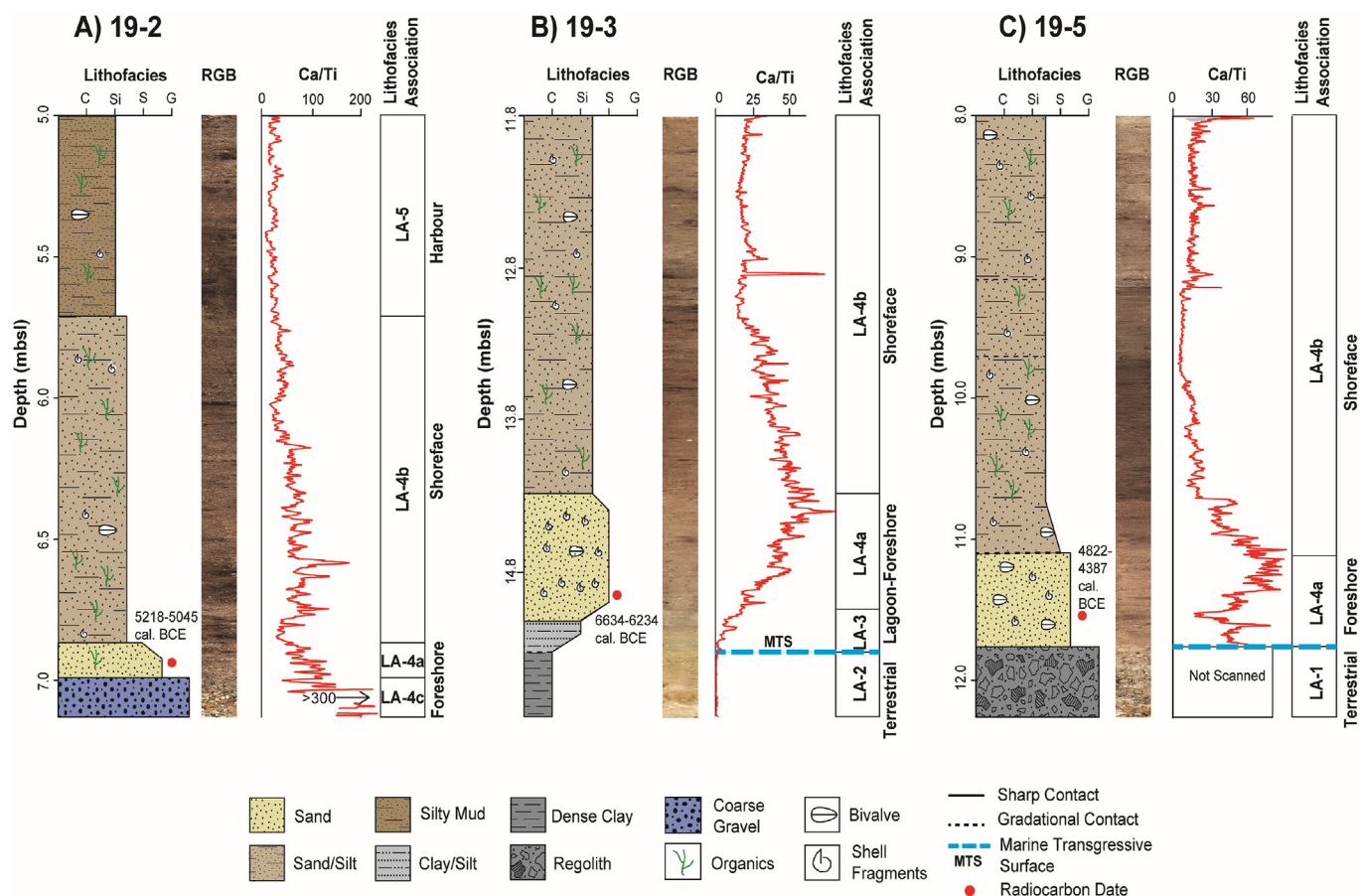


Fig. 7. Lithofacies logs, AMS ¹⁴C dates, RGB scan, and Ca/Ti ratio for cores 19-2 (A), 19-3 (B), 19-5 (C).

(<5/cc) (Fig. 5). *Diffflugid* thecamoebians were present in low abundance (<3/cc) in three cores (18-5, 19-1, 19-4). A bulk organic sample from LA-2 in core 19-1 (7.2 mbsl) yielded a Neolithic age of 7042-6747 cal. BCE (Fig. 5). Radiocarbon dates from above LA-2 in cores 18-5, 19-3, 19-4, 19-5, also indicate Neolithic ages, ranging from about 6500 to 6000 BCE (Fig. 6 c,d and 7 b,c).

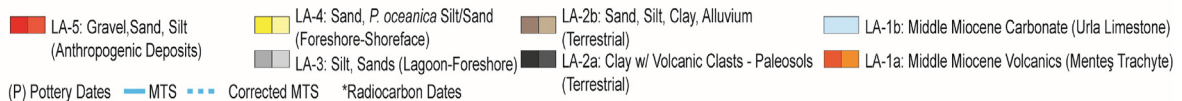
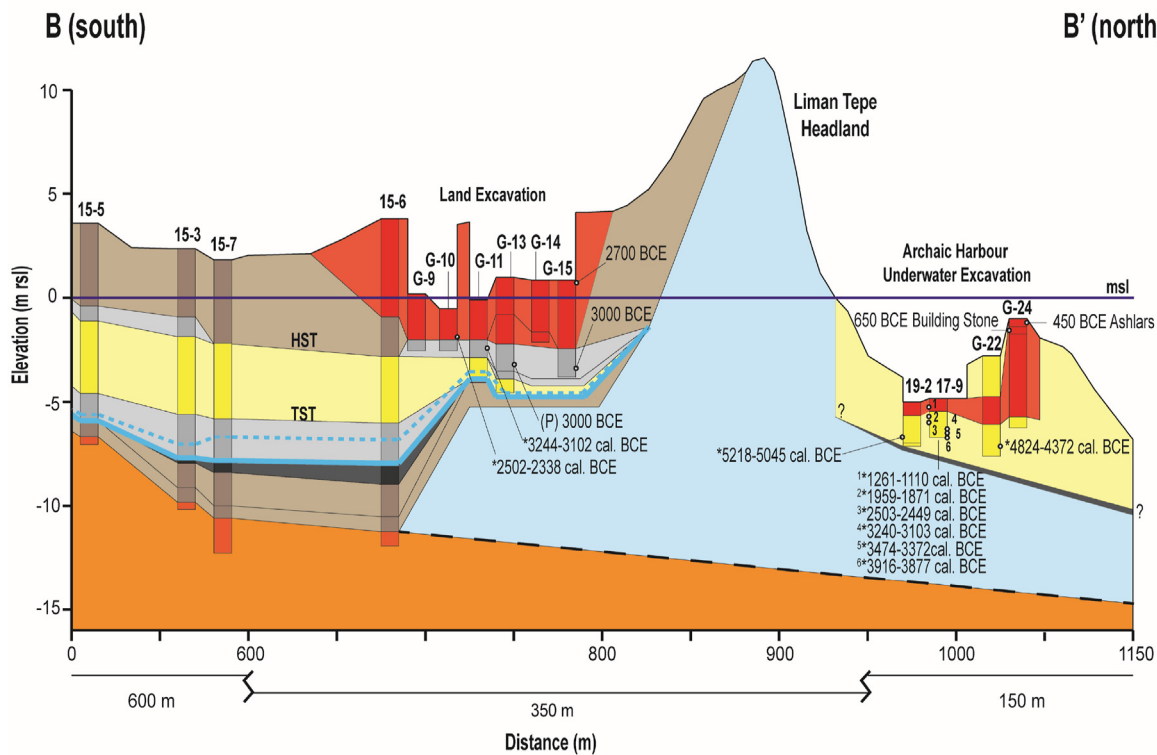
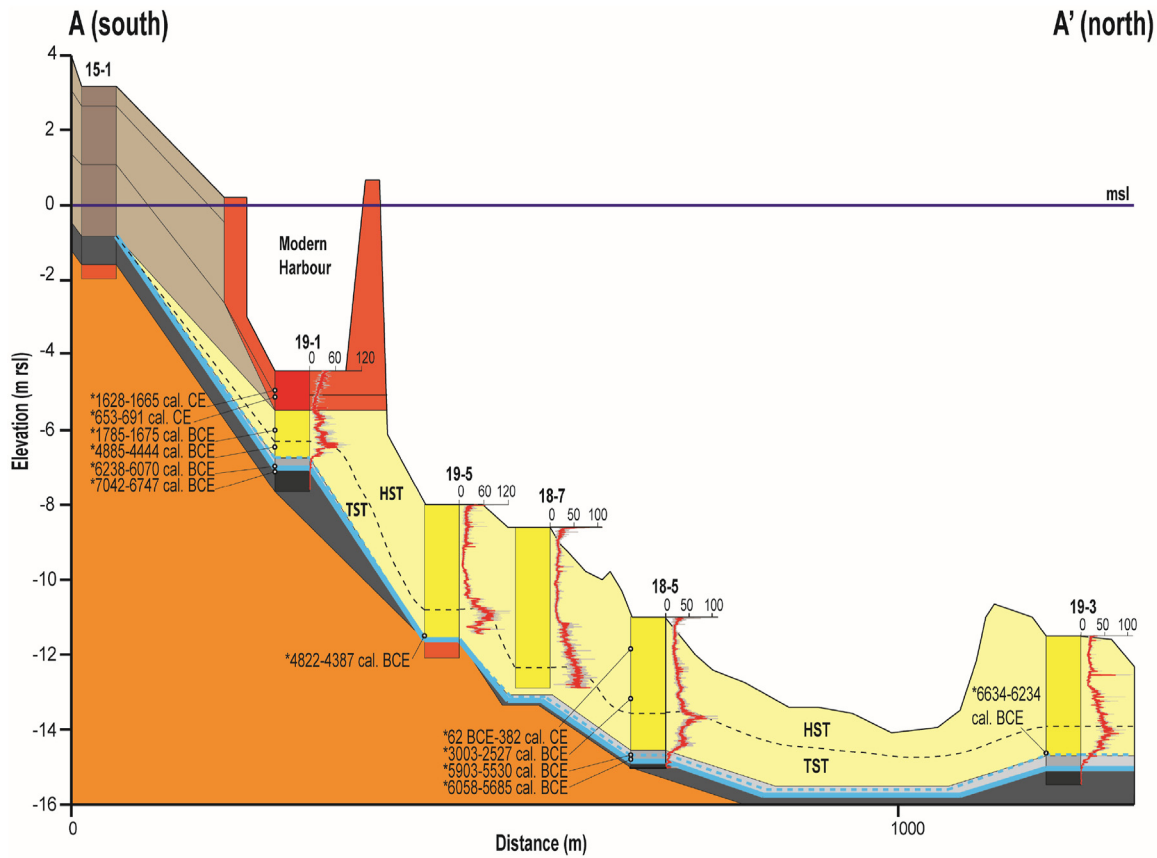
LA-2 is interpreted as a terrestrial mud deposit derived by weathering of the underlying volcanic saprolite and bedrock (i.e., LA-1). Ca/Ti values in LA-2 were low due to the abundance of Ti in the clays and volcanic regolith (Fig. 5). The low abundance of *Diffflugia* suggests deposition of thecamoebian tests by fluvial inputs to an inland lake or wetland (e.g., river palaeochannels; Fig. 2). The low abundance of foraminifera in LA-2 may record overflow of marine waters into wetlands or a coastal lake during storm events (e.g., Goodman et al., 2009). Goodman et al. (2008) had previously identified freshwater wetland facies in land cores at Liman Tepe, as defined by a high abundance of *Diffflugia* (25.5%, ~74.5/cc). Kayan et al. (2019) described a similar dark grey mud facies overlying alluvial silt and sand, which we provisionally correlate with LA-2 (Figs. 8 and 9). The lowermost terrestrial deposits identified by Goodman et al. (2008, 2009) (cores G-4, G-6, G-7, G-11) are also assigned to LA-2, based on their stratigraphic position below marine deposits and low foraminifera abundance (<2/cc). Radiocarbon dates from the overlying marine sediments (LA-3, LA-4) in cores G-4, G-7, G-8, and G-11, range in age from about 3200-2200 BCE (Figs. 8 and 9), indicating that the lowermost package of LA-2 sediments on land were deposited prior to the maximum marine transgression at ca. 4000 BCE. Offshore, the LA-2 sediments were deposited before 6600 BCE, as indicated by ages in the overlying

LA-3 sediments (Fig. 8a). A bulk ¹⁴C date near the top of LA-2 in core 19-1 yielded an age of 7042-6747 cal. BCE, indicating deposition in the Neolithic Period (Fig. 5). The contact between the lowermost terrestrial and overlying marine deposits identified by Goodman et al. (2008, 2009) and Kayan et al. (2019) represents the onshore extension of the MTS (Figs. 8 and 9). Kayan et al. (2019) and Goodman et al. (2008, 2009) identified an uppermost package of alluvial mud, silt, and sand facies (Figs. 8 and 9), which we assign as terrestrial deposits. This later sequence of terrestrial sediments records alluvial plain sedimentation after 4000 BCE and is assigned to LA-2b (Figs. 8 and 9).

4.2.3. LA-3 (lagoonal sediments)

LA-3 consisted of crudely stratified to laminated, clayey silt facies containing mollusk and gastropod shell fragments, overlying LA-2 across a transitional contact (Figs. 5, 6c and 7b). The unit contained disseminated fine organics but *Posidonia oceanica* fragments were absent. Foraminifera were in low abundance at the base of LA-3 (5-84/cc) and increased upward in the unit (162-200/cc) (Fig. 5). The dominant foraminifera genera were *Elphidium* (25 - >50%) and *Ammonia* (20 - >50%). In core 19-1, a few *Diffflugid* thecamoebians were present at the base of LA-3. A bulk organic sample in LA-3 in core 19-1 yielded an Early Neolithic age of 6238-6070 cal. BCE (Fig. 5) and mollusk shells in core 18-5 dated to 6058 to 5685 BCE and 5903-5530 cal. BCE (Fig. 6c).

LA-3 is interpreted as a low-energy coastal marsh or pond environment, based on its clayey-silt texture, overall low abundance of marine microfossils and presence of *Diffflugid* thecamoebians. The LA-2/LA-3 contact marks the MTS and a basin-wide



parasequence boundary, recording mid-Holocene marine flooding of the coastal plain (Figs. 8 and 9). We interpret the upwards increase in the foraminifera in LA-3 as transgressive flooding of a brackish marginal lake environment. The MTS is also identified by a distinct increase in Ca/Ti at the base of LA-3 (Figs. 5, 6c and 7b), which can be correlated throughout the basin (Fig. 8). The increase in Ca/Ti corresponds with an increased abundance of calcareous foraminifera and shell fragments, and reduced Ti in LA-3. Goodman et al. (2008, 2009) and Kayan et al. (2019) identified two similar foreshore and lagoonal silt and mud facies in land cores: one overlying LA-2 and the other overlying the LA-4 foreshore-shoreface deposits (Figs. 8 and 9). The land core lithofacies descriptions, however, are not sufficiently detailed for identification of foreshore versus lagoon facies, and so are grouped together here and are provisionally correlated with LA-3 (Figs. 8 and 9). Foreshore sands and lagoonal silt and mud deposits were also identified by Krezoski (2008) to the east of the Karantina Island (Fig. 9). These deposits infill a broad basin identified in seismic data (Fig. 4b and c), which records an extensive back-barrier lagoon that formed to the southeast of the island during the Neolithic (section 5.2).

4.2.4. LA-4 (foreshore-shoreface deposits)

LA-4 comprised a fining-upwards package of medium to fine sand and *Posidonia*-rich silt and mud facies (Figs. 5–7). Sand facies (LA-4a) were massive, poorly sorted, and contained sub-rounded to well-rounded mollusk shell fragments and scant marine organic matter. The overlying silt and mud facies (LA-4b) were massive to crudely stratified and contained abundant *Posidonia oceanica* matte layers and lenses (~0.1–1 cm in thickness). Foraminifera abundance was 258–1000/cc (Fig. 5), and the dominant genera were *Elphidium* (20–41%) and *Ammonia* (16–30%). LA-4 sediments yielded a wide range of ages from Late Neolithic to recent, as the sediments extend to the modern seafloor (e.g. cores 18-3: 2853–2378 cal. BCE to present) (Figs. 5–7).

The poorly sorted texture, presence of rounded mollusk fragments and absence of *Posidonia* fragments in LA-4a indicates deposition in high-energy, foreshore to upper shoreface environment. The relatively high abundance of foraminifera and *Posidonia* in the overlying LA-4b, in contrast, suggests deposition in a lower energy shoreface environment with conditions suitable for growth of seagrass meadows. In the modern environment at Liman Tepe, *Posidonia* meadows are extensive in water depths between 2 and 35 m and favour low water turbidity and low to moderate energy environments (Dural et al., 2012; Votruba et al., 2016). The Ca/Ti profiles reach peak values (>120) at the top of LA-4a at about 4000–3500 BCE in most cores (Figs. 5–7), corresponding with a transition from a high-energy foreshore to upper shoreface environment (Fig. 8a). This was followed by an overall decline in Ca/Ti, signaling increased terrestrial sediment inputs to the coast, as shorelines began to prograde during a HST after 4000 BCE (Fig. 8a). Goodman et al. (2008, 2009) and Kayan et al. (2019) described similar regressive shoreface deposits in land cores (Figs. 8 and 9). The shoreface deposits were dominated by *Elphidium*-*Ammonia* biofacies (defined by >10% *Elphidium*) and the presence of *Ammonia parkinsoniana* (Goodman et al., 2008, 2009).

Shallow water sediments, recording a range of foreshore and intertidal environments, were identified at or near the base of several marine cores (18-3, 19-2, 19-4; Figs. 6b, d and 7a) and were assigned to LA-4c. In core 19-4, underlying LA-4a, was a thin horizon (~20 cm) of disarticulated oyster shells (*Ostrea edulis*) and

shell fragments, overlain by a thin gravel layer, consisting of angular volcanic rock granules and pebble-sized clasts (Fig. 6d). The oyster shells and gravel contained abundant foraminifera (122–406/cc), dominated by *Elphidium* (25–29%) and *Ammonia* (23–29%). The oyster shell layer dated to 7th millennium BCE (6384–6000 cal. BCE; Fig. 6d) and may indicate a storm deposit, or possibly a refuse layer, recording human processing of oyster shells. In core 18-3, LA-4b rested on a ~50-cm-thick unit of shell-rich, cemented gravels (beachrock) across a sharp erosive contact (Fig. 6b). The unit records a shallow intertidal environment (ca. 5770–5406 cal. BCE), where groundwater flow permitted the cementation and production of beachrock (Vousdoukas et al., 2007). In core 19-2, LA-4c consisted of a thin (~15 cm) poorly-sorted basal gravel with rounded carbonate and volcanic rock granules and pebbles (Fig. 7a). The gravel layer is interpreted as a lag deposit, recording erosion of underlying sediments and bedrock in a beach or foreshore environment. Overall, erosional lag deposits were not a common feature of the foreshore deposits in LA-4.

4.2.5. LA-5 (harbour sediments, archaeological deposits)

LA-5 comprised a distinctive uppermost package of mud and fine silt with abundant marine mollusk shell fragments present in three cores (19-1, 17-9, 19-2) in the Archaic harbour basin (Figs. 5, 6a, and 7a). LA-5 sediments contained minor *Posidonia* lenses and fragments and abundant foraminifera (851–1094/cc). In cores 17-9 and 19-2, LA-5 sediments contained abundant pottery, including Archaic to Classical age (c. 7th - 4th c. BCE) vessel fragments and pottery sherds (Riddick et al., in review). In core 19-1 from the western harbour basin (Fig. 1b), LA-5 contained two sub-units: a lowermost muddy silt facies (LA-5a) and overlying fine-grained mud (LA-5b) separated by an erosional contact (Fig. 5a).

LA-5a represents harbour basin sediments deposited within a low-energy Archaic harbour basin (ca. 7–6th c. BCE) and a preceding proto-harbour embayment, which existed to the west of the Liman Tepe headland during the Middle-Late Bronze Age (ca. 2000–1200 BCE) (Riddick et al., in review). LA-5b records Byzantine to Modern era harbour deposits. An erosional hiatus at a depth of 70 cm in core 19-1 (LA-5a to 5b transition; Fig. 5a) may record dredging of the harbour basin prior to the 7th c. CE. On land, we also assign the uppermost surficial deposits containing archaeological materials to LA-5 (Fig. 8), recognizing that they were deposited in a range of terrestrial environments. Some of these surficial deposits were previously mapped as ‘anthropogenic sediments’ by Kayan et al. (2019) and contain archaeological strata ranging in age from Chalcolithic to present (Şahoğlu, 2015; Tuncel and Şahoğlu, 2018).

5. Discussion

5.1. RSL change

The revised RSL curve for Liman Tepe (Fig. 10) incorporates 31 new radiocarbon dates on terrestrial, intertidal and foreshore sea-level markers (Table 1). The glacio-hydro-isostatic sea-level curve of Lambeck (1995) and Aegean (sector “C”) curve of Vacchi et al. (2014) are shown for comparison. Kayan’s (1988) sea-level curve is also shown, as it was employed in a recent coastal reconstruction at Liman Tepe (Kayan et al., 2019). The new RSL curve conforms generally with Lambeck’s (1995) eustatic sea level curve prior to the inflection at ca. 4000 BCE, indicating a rapid early to middle Holocene rate of sea level rise of ~14 mmyr⁻¹ until ca. 6300 BCE,

Fig. 8. Core transects (A-A’ and B-B’; Fig. 1b) showing correlation of marine lithofacies assemblages with onshore core data. Ca/Ti profiles shown in A-A’. Cores redrawn from Goodman et al. (2008, 2009) and Kayan et al. (2019). AMS ¹⁴C dates compiled in Table 1. In transect B–B, LA-3 includes lagoon and foreshore facies identified by Goodman et al. (2008, 2009) and Kayan et al. (2019). Marine transgressive surface (MTS) corrected for post-depositional compaction indicated by dashed blue line. HST = high-stand systems tract, TST = transgressive systems tract. (For interpretation of the references to colour in this figure legend, the reader is referred to the Web version of this article.)

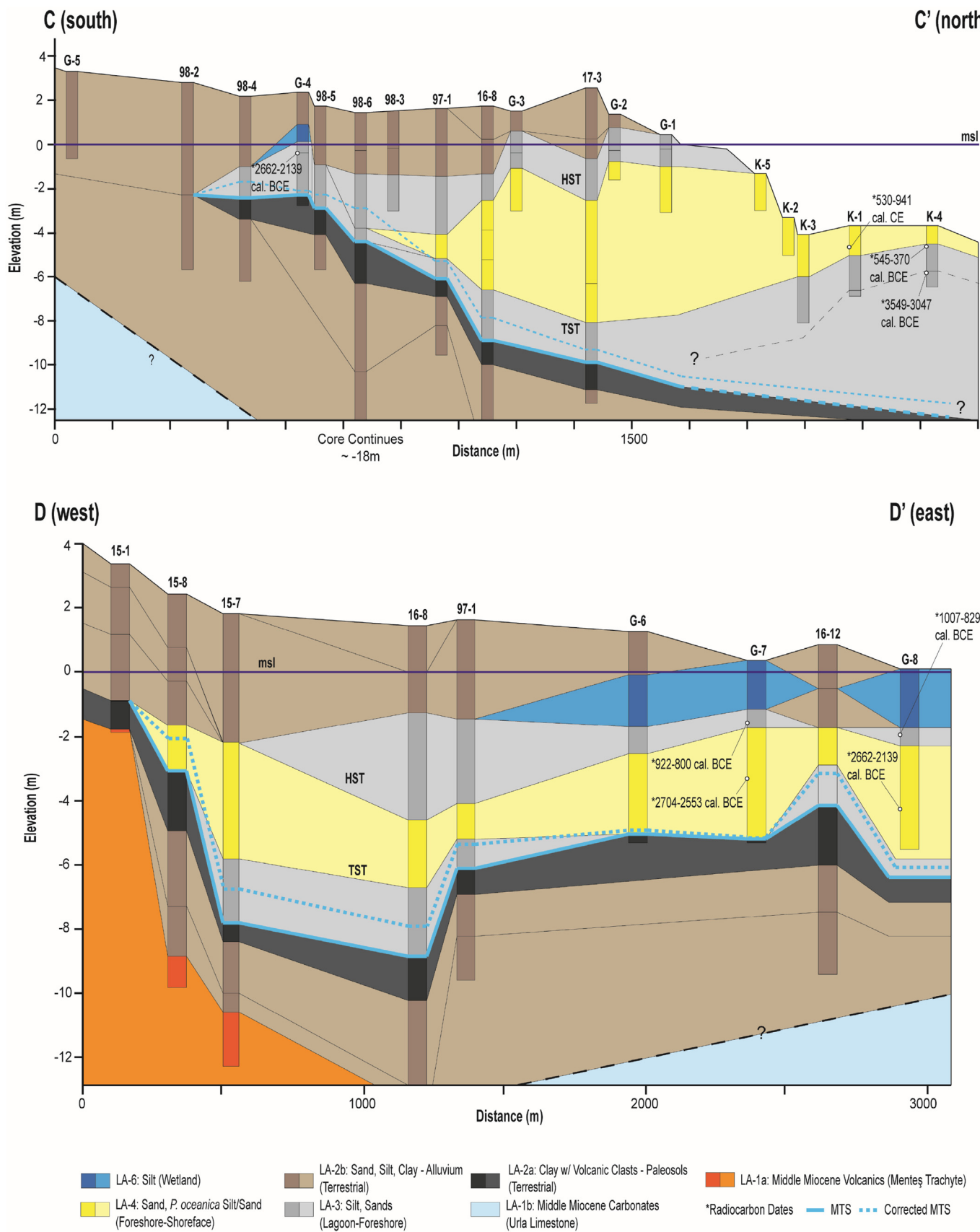


Fig. 9. Core transects (C–C’ and D–D’; Fig. 1b) showing correlation of marine and land core data. Cores redrawn from Krezoski (2008), Goodman et al. (2008, 2009), and Kayan et al. (2019). LA-3 includes lagoon and foreshore facies identified in previous land coring work. Marine transgressive surface (MTS) corrected for post-depositional compaction indicated

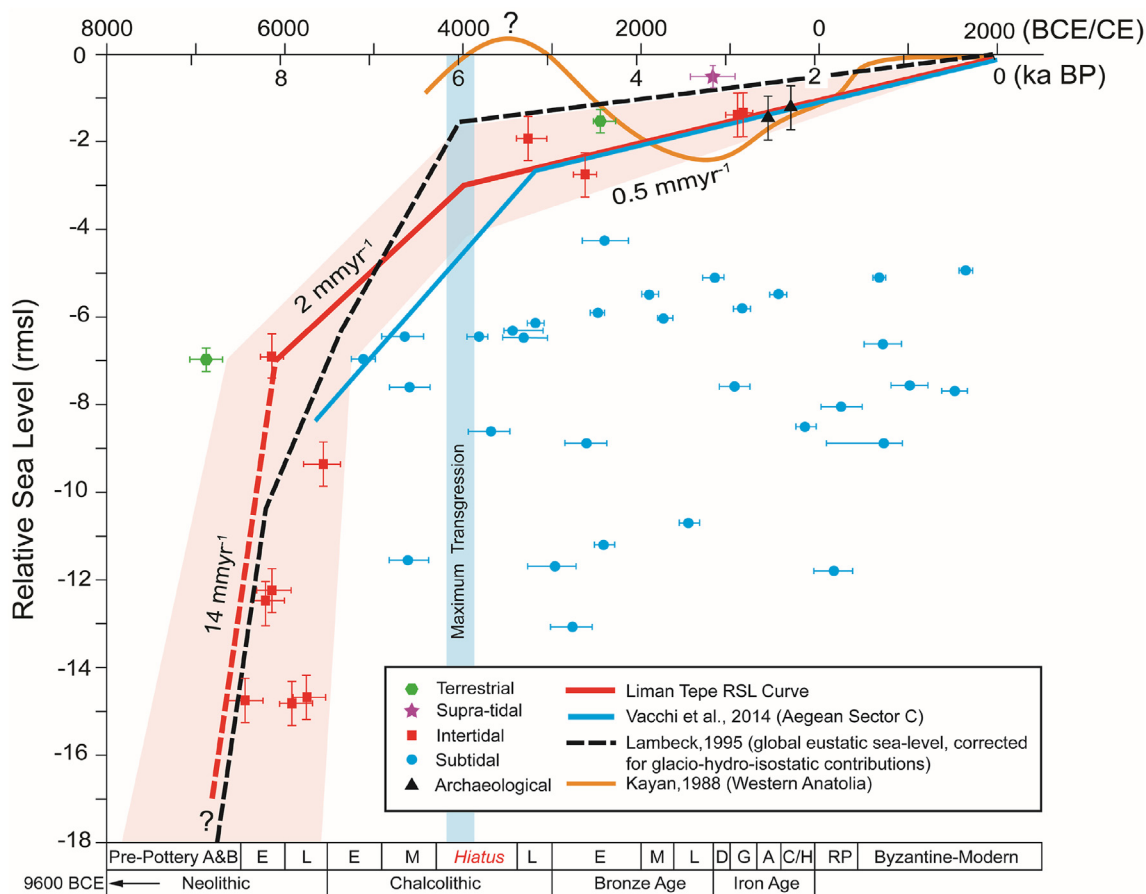


Fig. 10. Liman Tepe relative sea level (RSL) curve (red line) based on new sea level indicators and previous markers with recalibrated ages from Goodman et al. (2008, 2009) (Table 1). All RSL indicators corrected for autocompaction. Eustatic sea level curve (corrected for hydro-glacio-isostatic contributions) of Lambeck (1995), and RSL curves of Kayan (1988) and Vacchi et al. (2014) shown for comparison. The maximum marine transgression at ca. 4000 BCE coincided with a hiatus in Chalcolithic settlement activity at Liman Tepe. (For interpretation of the references to colour in this figure legend, the reader is referred to the Web version of this article.)

followed by a deceleration to $\sim 2 \text{ mmyr}^{-1}$, during the final phase of deglaciation (Lambeck et al., 2014). From ca. 4000 BCE to present, RSL rose at a lower rate of about $\sim 0.5 \text{ mmyr}^{-1}$, in parallel with the regional Aegean curve constructed by Vacchi et al. (2014) for the sector C Aegean microplate (Fig. 10).

Both the Liman Tepe RSL curve and that of Vacchi et al. (2014) lie below the eustatic sea-level curve of Lambeck (1995), indicating regional tectonic controls on sea level. We also note that the segment of our RSL curve for the period prior to ca. 3500 BCE lies above the Vacchi et al. (2014) curve (Fig. 10), indicating a departure from the general trend of RSL in the Aegean sector “C”. The RSL inflection point at ca. 4000 BCE is generally attributed to the deceleration in post-glacial sea level rise as global ice volumes stabilized (Fleming et al., 1998; Lambeck et al., 2014). The difference between the local RSL and the eustatic curve of Lambeck (1995) ($\sim 1.5 \text{ m}$ at ca. 4000 BCE) may record ongoing tectonic subsidence in the Bay of Izmir, previously estimated at 1 mmyr^{-1} (Aksu et al., 1990). The $\sim 1.5 \text{ m}$ difference between the curves, however, suggests a lower rate of subsidence from 4000 BCE to present, on the order of $\sim 0.25 \text{ mmyr}^{-1}$ (Fig. 10). Some component of the subsidence may be due to uncompensated sediment autocompaction in unconsolidated sediments below cores that do not penetrate fully to bedrock. Coastal subsidence in the Bay of Izmir is also likely driven

by ongoing basin extension at the western end of the Gediz Graben (Çiftçi, and Bozkurt, 2009) and increased sediment loading (Reynolds et al., 1991) due to rapid coastal progradation after 4000 BCE. Multi-beam mapping and sub-bottom seismic studies in the Bay of Izmir have identified active faults in basin floor sediments, which have been interpreted as normal and strike-slip faults produced by Holocene basin extension (Çoşkun et al., 2017). Further detailed analysis of RSL markers from both inshore and offshore areas are needed to confirm and quantify basin subsidence on the coastline.

The RSL curve of Kayan (1988) predicts a middle Holocene highstand $\sim 0.5 \text{ m}$ above modern between ca. 4000–3000 BCE, followed by a $>2\text{-m}$ drop in sea levels and a relative lowstand at about 1200 BCE (Fig. 10). Kayan’s (1988) sea level reconstruction was based on beachrock elevations from the Datça Peninsula (Knidos harbour) and has been applied broadly to the interpretation of the palaeogeography of coastal sites in western Turkey (see Kayan, 2019). The high-stand event is not recognized in our observations at Liman Tepe, which indicate sea levels below modern after ca. 4000 BCE (Fig. 10). A single supra-tidal marker from Goodman et al. (2009) lies about 1 m above the RSL curve (-0.5 mbsl , ca. 1200 BCE; Fig. 10). The marker was a shell fragment and may be an outlier radiocarbon age, or may indicate a coastal lake impounded above

by dashed blue line. HST = high-stand systems tract and TST = transgressive systems tract. The marine transgressive limit is indicated by the maximum shoreward extent of marine deposits in C–C. (For interpretation of the references to colour in this figure legend, the reader is referred to the Web version of this article.)

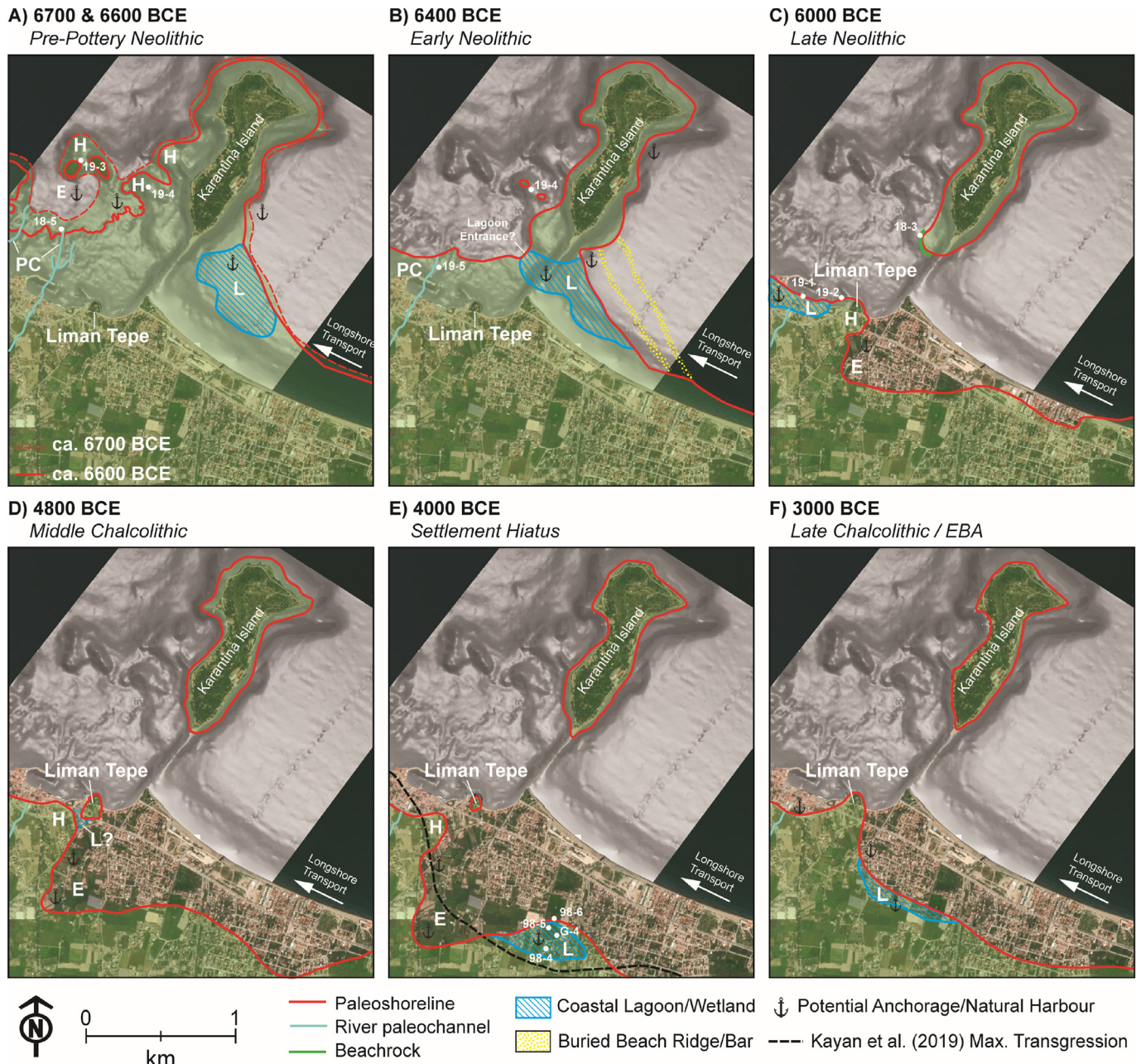


Fig. 11. Reconstructed Neolithic to EBA (ca. 6700–3000 BCE) coastal palaeogeography of Liman Tepe. A–D: Transgressive systems tract (TST). Coastal plain inundated during mid-Holocene phase of rapid sea level rise. E. Maximum marine transgression ~1 km inland at ca. 4000 BCE. Liman Tepe headland was a small island separated from mainland. Marine transgressive limit of [Kayan et al. \(2019\)](#) shown for comparison. F. High-stand systems tract (HST). Deceleration in sea level rise resulted in positive sediment budget on coast. Progradation of coastline with development of barrier-lagoon systems. Areas of high archaeological potential indicated: H = headlands/promontories (potential settlement locations), E = embayments (anchorage sites), L = lagoons/wetlands (anchorage, resources), PC = river palaeochannels (floodplain habitats and resources).

sea level. Sea levels above modern between 4000 and 3000 BCE ([Fig. 10](#)) are also not supported by our palaeoshoreline reconstruction, as they result in a marine transgressive limit that is farther inland than observed in land core data (e.g. [Goodman et al., 2009](#); [Kayan et al., 2019](#)) ([Figs. 8, 9 and 11e](#)).

5.2. Holocene depositional environments and palaeogeography

Five distinct lithofacies assemblages have been recognized in marine cores and correlated with onshore stratigraphic data ([Figs. 8 and 9](#)). The lithofacies stacking patterns indicate two depositional phases, resulting from changes in RSL ([Fig. 10](#)), sediment supply and

accommodation space on the coast ([Catuneanu, 2002](#)). A TST and rapid phase of sea level rise obtained until ca. 4000 BCE and was followed by a HST ([Goodman et al., 2008](#)), with the deceleration in sea level rise and decrease in accommodation space on the coast. Changes in the coastal palaeogeography and environments during these phases are shown in [Fig. 11](#) and discussed in the following sections.

5.2.1. Transgressive systems tract (TST)

The TST is represented by a lowermost sediment package of marine sediments, consisting of a coarsening-upward sequence of marine lagoonal and foreshore facies overlain by upper shoreface

deposits (Figs. 8 and 9). The maximum transgression extended approximately 1 km inland of the present shoreline at ca. 4000 BCE (Fig. 11e). The marine limit is in general agreement with previous work (Goodman et al., 2008; Kayan et al., 2019) and the new palaeogeographic maps provide additional details on the configuration of headlands and coastal embayments, formed by the inundation of the coastal plain (Fig. 11). The preservation of relict palaeoshoreline features and palaeochannels to the west of Karantina Island (Figs. 2 and 3) suggests that the low-relief coastal plain was submerged rapidly.

At 6700–6600 BCE, RSL was ~14–16 m below present and the shoreline was >500 m seaward of the modern coast (Figs. 10 and 11a). The shoreline position at 6600 BCE is coincident with a break in slope at –11 to –12 m in the modern bathymetry (Fig. 2b). The low relief (1.5–3 m) scarp defining the palaeoshoreline (Figs. 3b, c) may record a brief still-stand event, or possible structural control on the shoreline position by an underlying bedrock ridge, as the bedrock surface is at a relatively shallow depth below Holocene sediments on the west side of the study area (Fig. 8a). The relict river channels terminate at the palaeoshoreline (Fig. 2), which suggests that the preserved floodplain dates to ca. 6700–6400 BCE. At this time, Karantina Island was a broad headland with an extensive western coastal promontory that formed a sheltered embayment to the north of Liman Tepe (Fig. 11a). To the southeast of Karantina Island, an extensive barrier-lagoon system was formed as the coastline stepped landward (Figs. 11a, b). The lagoon may have been open to the sea at its western extent, as indicated by a bathymetric low (Fig. 2a) on the west side of the causeway. The northwest-trending ridges identified in seismic data (Fig. 4) record buried transgressive barriers, which were drowned-in-place by shoreline overstepping (Rampino and Sanders, 1980; Mellett and Plater, 2018).

The western coastal promontory of Karantina Island was progressively inundated after 6600 BCE forming a series of small islands (Fig. 11a and b). Intertidal gravel deposits containing oyster shells (core 19-4, 6384–6000 cal. BCE) may record Early Neolithic shell gathering and processing (Çakırlar, 2015) on the western shore of Karantina Island (Figs. 6d and 11b). The western shore of the island continues to be a habitat for the European flat oyster (*Ostrea edulis*) and fan mussel (*Pinna nobilis*), which are gathered for local consumption (Lök and Acarlı, 2006).

By 6000 BCE, the coastline had transgressed close to its modern position and Karantina Island was separated from the mainland (Fig. 11c). A marine embayment existed to the southeast of the Liman Tepe headland and a coastal lagoon was present on the west side of the promontory (Fig. 11c), as indicated by LA-3 deposits in core 19-1 (Fig. 5). On the west side of Karantina island, at the location of core 18-3, beachrock formed in an intertidal environment (5770–5406 cal. BCE) (Fig. 11c). By the Middle Chalcolithic period (ca. 4800 BCE), the coastline had transgressed landward ~800 m of the modern shore and the Liman Tepe promontory was separated from the mainland by a shallow wetland (Fig. 11d) (Goodman et al., 2008).

5.2.2. High-stand systems tract (HST)

At 4000 BCE, the rate of sea level rise decreased (Fig. 10) and accommodation space was outpaced by sediment supply on the coast, resulting in a net positive sediment budget and switch to a HST (Figs. 8 and 9). The coastline prograded through the accretion of linear beach barriers backed by shallow lagoons (Goodman et al., 2008). The HST is recorded by an upwards-fining succession of shoreface sands overlain by lagoonal and wetland facies (Figs. 8 and 9). At the beginning of the HST, the Liman Tepe headland was a small island with a large coastal embayment to the southeast (Fig. 11e). A coastal lagoon was present on the eastern side of the

embayment, as indicated by the presence of silt and mud facies in cores 98-4, 98-5, 98-6 and G-4 (Figs. 9 and 11e). Between 4000 and 3000 BCE, the coastal embayment was progressively infilled, as the shoreline prograded rapidly to a position 200–400 m inland of the modern coast (Fig. 11e). The Liman Tepe headland was reconnected with the mainland forming a small marine embayment in the west and shore-parallel lagoon to the southeast (Fig. 11f).

5.3. Archaeological implications

The new palaeogeographic reconstructions provide important insights into the prehistoric settlement history of Liman Tepe. An unresolved archaeological problem was the absence of Neolithic settlement layers on the land archaeological site (Fig. 1c). Palaeogeographic reconstructions show that prior 6400 BCE, Liman Tepe was >500 m inland of the coast (Fig. 11a, b), which may explain the lack of evidence for Neolithic habitations. The site became a coastal promontory during the Late Neolithic (before 6000 BCE), when the sea had transgressed close the modern shoreline position (Fig. 11c). Between 6700 and 4000 BCE, the shoreline advanced ~2 km inland at a rate of 0.2–0.75 myr⁻¹, rapidly transforming the coastal landscape (Fig. 11a–e). The Early Holocene coastal plain was inundated over a period of about 700 years. These rapid changes in the shoreline position and coastal environments would have been perceptible to people living and gathering resources on the coast and would likely have required short-term adaptations to rising sea levels. Given the inland location of Liman Tepe at the beginning of the Neolithic, coastal headlands, and sheltered bays on the west coast of Karantina Island may have been more favourable locations for coastal settlement (Figs. 11a, b). During the Neolithic (ca. 6700 BCE), the westernmost headland of Karantina Island was ~4–5 m above sea level (Fig. 3c) and enclosed a small (0.3 km²) embayment with a river mouth and floodplain to the south (Fig. 11a). The embayment would have provided well-protected anchorage areas and the coastal promontory was larger in extent than the Liman Tepe headland settled during the Middle Chalcolithic phase (Fig. 11). The promontory and coastal embayment, now submerged in water depths of 8–16 m (Figs. 2b and 3c) are identified as areas with high archaeological potential for submerged prehistoric sites.

The presence of a river system and alluvial plain with wetland resources at Liman Tepe (Figs. 2 and 11a) would have been highly attractive to Neolithic settlers and was a potential factor in the founding of the Chalcolithic and EBA settlements at Liman Tepe (Goodman et al., 2008). The floodplain and low-lying coastal wetlands would have provided a perennial water source for settlement and agriculture, and rich coastal habitats for resource gathering. The volcanic soils of the alluvial plain would also have provided fertile lands for farming and domestic livestock. Evidence from nearby sites in Izmir (e.g., Yeşilova; Fig. 1a), suggest that riverine and marine shellfish gathering was a major component of Neolithic and Chalcolithic subsistence strategies (Derin, 2007; Çakırlar, 2015). The presence of oyster shells in core 19-4, representing a possible midden deposit or storm layer (Fig. 6d), indicates an important shellfish resource on the coast during the Neolithic period. The river floodplain would have also provided a source of raw materials (i.e. clay) for settlement construction. Coring at location 19-1 revealed a thick, clay-rich palaeosol developed on volcanic regolith (Fig. 5). These deposits are the likely source of clay used in the prehistoric mud brick (wattle-and-daub) architecture at Liman Tepe (Tuncel and Şahoğlu, 2018).

On the Liman Tepe headland (Fig. 1c), the earliest settlement layers date to the Middle Chalcolithic (ca. 4600–4200 BCE). This first phase of settlement was followed by a 600–1000-year hiatus in activity before a final Late Chalcolithic re-occupation of the site (Tuncel and Şahoğlu, 2018). Similar hiatuses have been recognized

in the Chalcolithic settlement phases of other sites in the region, but the reasons for the hiatus at Liman Tepe are not well understood (Tuncel and Şahoğlu, 2018). Palaeogeographic reconstructions show that during Middle Chalcolithic (ca. 4800 BCE), the headland was connected to the mainland (possibly by a sand tombolo) and was backed by a shallow water area (<1 m), possibly a coastal wetland (Fig. 11d). During the time of the settlement hiatus, the shoreline advanced to the maximum marine limit (about 1 km inland, ca. 4000 BCE) and the northernmost point on the headland became a small island, located ~300 m offshore (Fig. 11e). The inundation of the headland by rising sea levels may have caused the migration of Middle Chalcolithic settlement to the mainland, which could explain the apparent gap in human activity during this period. The area to the southwest of Liman Tepe, now part of the modern town of Iskele, was located on the mainland coast opposite the island at ca. 4000 BCE (Fig. 11e). This area has high potential for a possible Chalcolithic settlement.

The archaeological evidence for seafaring activity at Liman Tepe indicates diverse trade connections with the wider Aegean and the Anatolian hinterlands during the Chalcolithic and EBA periods (Şahoğlu, 2005; Erkanal, 2017). It has been proposed that sheltered coastal embayments and lagoons to the west and southeast of the Liman Tepe headland (Fig. 11f) were anchorage sites during these settlement phases (Goodman et al., 2009; Kayan et al., 2019; Riddick et al., in review). The palaeoshoreline maps support these interpretations, showing that the coastal lagoon on the east side of the headland would have been well-protected from the dominant north and northwest winds (Figs. 1b and 11f). On the western side of the headland, the elemental geochemistry of the LA-5 silty mud lithofacies (core 17-9; Fig. 6a) indicates the presence of a low-energy marine embayment formed in the lee of the rocky headland (Riddick et al., in review). The embayment has been interpreted as a Late Bronze 'proto-harbour' basin and pre-cursor to Clazomenae's large (>5 ha), semi-closed Archaic (ca. 7th c. BCE) harbour facility. During the Middle to Late Bronze, the shoreline of the proto-harbour embayment was about 100 m inland of the modern coast, in the area now occupied by the town of Iskele (Figs. 1b and 11f). The former marine embayment has high potential for discovery of mid-late Bronze anchorage sites and evidence for maritime trade activity (Fig. 11f). The inland position of the prehistoric shoreline relative to the modern coast (Fig. 11) also explains the absence of Late Chalcolithic-EBA pottery in the sediments below Archaic harbour basin deposits (Riddick et al., in review).

5.4. Future work

The coastal palaeogeographic reconstructions (Fig. 11) provide new baseline data that will guide future exploration of the prehistoric underwater archaeological potential at Liman Tepe. The submerged coastal promontories and landscape features (river palaeochannels, palaeoshorelines) on the west side of Karantina Island are primary targets for future underwater investigations (Fig. 2). The Holocene sediment thickness (1–4 m; Fig. 8a) presents a challenge for underwater archaeological exploration but does not preclude future discovery of submerged prehistoric sites. Detection of potential buried sites will require detailed, site-scale geophysical surveys and underwater coring. Marine geophysical mapping (e.g. marine magnetic, resistivity surveys) and sub-bottom profiling will assist in determining the Holocene sediment thickness and presence of potential buried sites (Müller et al., 2009; Missiaen et al., 2017). Seismic surveys were not completed on the west side of Karantina Island in this study due to heavy wave conditions, which prevented surveying with surface-towed instruments. Planned future work will employ an AUV (autonomous underwater vehicle) equipped with sub-bottom profiler and side-scan sonars that can

be deployed under any sea state. AUVs can be programmed to systematically grid map the seabed and sub-bottom stratigraphy with high-resolution imaging capabilities (Missiaen et al., 2017; Batchelor et al., 2020). Diver reconnaissance of the palaeoshoreline and palaeochannel margins (e.g. using diver propulsion systems) will also target areas where active slumping of Holocene deposits (Fig. 3) may have exposed sediment outcrops and prehistoric cultural materials. The confirmation of prehistoric sites will ultimately require underwater archaeological excavations using dredging methods.

6. Summary

Previous geoarchaeological studies at Liman Tepe have focused on the land and nearshore sediment record with a limited radiocarbon chronology (Goodman et al., 2008, 2009; Krezoski, 2008; Kayan et al., 2019). In this paper, we have assembled a large geoscience database, including 40 marine and land cores, 45 radiocarbon dates and geophysical data (>600-line-km), to reconstruct the prehistoric coastal palaeogeography of Liman Tepe (Fig. 11). The Neolithic to Late Chalcolithic was a period of rapid sea level rise and marine transgression ($0.2\text{--}0.75\text{ myr}^{-1}$). From 6700 to 4000 BCE, the shoreline advanced >2 km inland, inundating the coastal plain and submerging coastal headlands and alluvial plain on the western shore of Karantina Island (Fig. 11a–e). After 4000 BCE, the global rate of sea level rise decelerated, and the coastline prograded under a HST, by the accretion of linear lagoon-barrier systems.

Our results are in general agreement with the findings of previous coastal reconstructions at Liman Tepe (Goodman et al., 2008, 2009; Kayan et al., 2019) but provide important new details of the shoreline positions during the Neolithic and Chalcolithic settlement phases. The revised RSL curve for Liman Tepe indicates that sea levels were below modern during the period ca. 6700 BCE to present with no evidence for Holocene levels above modern. The new palaeoshoreline mapping identifies several areas with high underwater archaeological potential, including locations favourable for Neolithic settlement (i.e. coastal headlands, palaeoshorelines) and better resolves the locations of coastal embayments and lagoons, which may have served as prehistoric anchorage sites (Goodman et al., 2009; Riddick, 2021). The mapping also identifies relict river channels on a submerged coastal floodplain, which would have been attractive environments for Neolithic settlers as coastal habitation sites with perennial freshwater and wetland resources.

Author contributions

NLR and JIB conducted data analysis, figure drafting, primary writing and revising of the manuscript. NLR, JIB, VŞ and HE conceived the research concept and objectives. Fieldwork was conducted by NLR, JIB, İT, YA and GMK. BNGT and EGR contributed micropalaeontological data and interpretations and JJG processed the seismic data. All authors contributed to the data interpretation, writing, and editing of the manuscript.

Data availability

Micropalaeontological data used in this study are available at: <https://data.mendeley.com/datasets/hm9x276fpj/1> an open-source online data repository hosted at Mendeley Data (Riddick et al., 2021b).

Declaration of competing interest

The authors declare that they have no known competing

financial interests or personal relationships that could have appeared to influence the work reported in this paper.

Acknowledgements

Research work was conducted under permits from the Turkish Ministry of Culture and Tourism. Research was funded by Natural Sciences and Engineering Research Council (NSERC) of Canada grant (RGPIN-2014-05829) to JIB and grants from the Turkish Ministry of Culture and Tourism, Institute for Aegean Prehistory (INSTAP), TÜBİTAK (108K263; 114K266) and Ankara University, to VŞ and HE. We also gratefully acknowledge the funding and support of the Turkish Historical Society (TTK), İzmir Metropolitan Municipality, Turkish Institute of Nautical Archaeology (TINA), the Koç Foundation, and the logistical support of the Urla Municipality. NLR was supported by a NSERC Canada Graduate Scholarship. We thank the students and staff of the Ankara University Mustafa V. Koç Center for Maritime Archaeology (ANKÜSAM), İzmir Region Excavations and Research Project (IRERP), for field and logistical support and Seequent (Canada) for a Geosoft academic software grant. We thank two anonymous reviewers and the editor for constructive reviews. We dedicate this paper to the memory of dear colleague, mentor and friend, Prof. Dr. Hayat Erkanal (1940–2019).

References

- Agostini, S., Tokcaer, M., Savaşçın, M.Y., 2010. Volcanic rocks from Foça-Karaburun and Ayvalık-Lesvos grabens (western Anatolia) and their petrogenetic-geodynamic significance. *Turk. J. Earth Sci.* 19 (2), 157–184.
- Aksu, A.E., Konuk, T., Ulug, A., Duman, M., Piper, D.J.W., 1990. Quaternary tectonic and sedimentary history eastern Aegean Sea and shelf areas. *Jeofizik* 4 (1), 3–35.
- Aksu, A.E., Piper, D.J.W., Konuk, T., 1987. Late Quaternary tectonic and sedimentary history of outer Izmir and Candarli Bays, western Turkey. *Mar. Geol.* 76, 89–104.
- Allen, J.R.L., 2000. Holocene coastal lowlands in NW Europe: autocompaction and the uncertain ground. *Geological Society, London, Special Publications* 175 (1), 239–252.
- Anthony, E.J., Marriner, N., Morhange, C., 2014. Human influence and the changing geomorphology of Mediterranean deltas and coasts over the last 6000 years: from progradation to destruction phase? *Earth Sci. Rev.* 139, 336–361.
- Aucelli, P.P., Mattei, G., Caporizzo, C., Cinque, A., Amato, L., Stefanile, M., Pappone, G., 2021. Multi-proxy analysis of relative sea-level and paleoshoreline changes during the last 2300 years in the Campi Flegrei caldera. *Southern Italy. Quat. Int.* 602, 110–130.
- Bailey, G.N., Flemming, N.C., 2008. Archaeology of the continental shelf: marine resources, submerged landscapes and underwater archaeology. *Quat. Sci. Rev.* 27 (23–24), 2153–2165.
- Bailey, G.N., Harff, J., Sakellariou, D., 2017. Archaeology and palaeolandscapes of the continental shelf: an introduction. In: *Under the Sea: Archaeology and Palaeolandscapes of the Continental Shelf*. Springer, pp. 1–17.
- Bailey, G.N., Jöns, H., Galanidou, N., Peeters, H., Mennenga, M. (Eds.), 2020. *The Archaeology of Europe's Drowned Landscapes*, vol. 35. Springer Nature.
- Batchelor, C.L., Montelli, A., Ottesen, D., Evans, J., Dowdeswell, E.K., Christie, F.D., Dowdeswell, J.A., 2020. New insights into the formation of submarine glacial landforms from high-resolution Autonomous Underwater Vehicle data. *Geomorphology* 370, 107396.
- Beck, J., Koutsoumba, D., Sakellariou, D., Surdez, M., Anselmetti, F., Papadopoulos, N., Morfis, I., Panagiotopoulos, I., Rousakis, G., Oikonomou, D., Simyrdanis, K., 2021. Searching for neolithic sites in the bay of kiladha, Greece. *Quat. Int.* 584, 129–140.
- Becker, J.J., Sandwell, D.T., Smith, W.H.F., Braud, J., Binder, B., Depner, J.L., et al., 2009. Global bathymetry and elevation data at 30 arc seconds resolution: SRTM30_PLUS. *Mar. Geodes.* 32 (4), 355–371.
- Benjamin, J., Rovere, A., Fontana, A., Furlani, S., Vacchi, M., Inglis, R.H., Galili, E., Antonioli, F., Sivan, D., Miko, S., Mourtzas, N., Felja, I., Meredith-Williams, M., Goodman-Tchernov, B., Kolaiti, E., Anzidei, M., Gehrels, R., 2017. Late Quaternary sea-level changes and early human societies in the central and eastern Mediterranean Basin: an interdisciplinary review. *Quat. Int.* 449, 29–57.
- Blaauw, M., Christen, J.A., 2011. Flexible paleoclimate age-depth models using an autoregressive gamma process. *Bayesian Analysis* 6 (3), 457–474.
- Boyce, J.I., Kresoski, G.M., Erkanal, H., Sahoglu, V., Goodman, B.N., Artzy, M., 2007. Shallow Water Mapping of a Submerged Archaic-Age Harbor at Liman Tepe, Turkey Using Data-Fused Magnetic and Side-Scan Data. *Geological Society of America, Annual Meeting, Denver, USA*.
- Bozkurt, E., Sozbilir, H., 2004. Tectonic evolution of the Gediz Graben: field evidence for an episodic, two-stage extension in western Turkey. *Geol. Mag.* 141 (1), 63–79.
- Brain, M.J., Kemp, A.C., Horton, B.P., Culver, S.J., Parnell, A.C., Cahill, N., 2015. Quantifying the contribution of sediment compaction to late Holocene salt-marsh sea-level reconstructions, North Carolina, USA. *Quat. Res.* 83 (1), 41–51.
- Catuneanu, O., 2002. Sequence Stratigraphy of clastic systems: concepts, merits, and pitfalls. *J. Afr. Earth Sci.* 35 (1), 1–43.
- Çakırlar, C., 2015. Adaptation, identity, and innovation in Neolithic and Chalcolithic Western Anatolia (6800–3000 cal. BC): the evidence from aquatic mollusk shells. *Quat. Int.* 390, 117–125.
- Çiftçi, N.B., Bozkurt, E., 2009. Pattern of normal faulting in the Gediz graben, SW Turkey. *Tectonophysics* 473 (1–2), 234–260.
- Clark, P.U., Dyke, A.S., Shakun, J.D., Carlson, A.E., Clark, J., Wohlfarth, B., Mitrovica, J.X., Hostetler, S.W., McCabe, M.A., 2009. The last glacial maximum. *Science* 325 (5941), 710–714.
- Conolly, J., Obie, M., 2021. The archaeology of inundated cultural landscapes in freshwater lake systems: preliminary insights from a multi-methods study in the Kawartha Lakes Region, Ontario. *J. Marit. Archaeol.* 1–18.
- Çoşkun, E., Balas, L., 2018. sea level changes in Izmir bay. *Int. J. Eng. Res. Dev.* 14 (9), 68–73.
- Çoşkun, S., Dondurur, D., Cifci, G., Aydemir, A., Gungor, T., Drahor, M.G., 2017. Investigation on the tectonic significance of Izmir, Uzunada Fault Zones and other tectonic elements in the Gulf of Izmir, western Turkey, using high resolution seismic data. *Mar. Petrol. Geol.* 83, 73–83.
- Dalrymple, R.W., James, N.P., 2010. Introduction to siliciclastic facies models. *Facies models* 4, 59–72.
- Derin, Z., 2007. Neolithic shellfish gathering at Yeşilova: an ethnoarchaeological view. *Ethnoarchaeological Investigations in Rural Anatolia* 45.
- Duman, M., Avci, M., Duman, S., Demirkurt, E., Duzbastilar, M., 2004. Surficial sediment distribution and net sediment transport pattern in Izmir Bay, western Turkey. *Continental Shelf Res.* 24 (9), 965–981.
- Dural, B., Aysel, V., Demir, N., Erduğan, H., 2012. The status of sensitive ecosystems along the Aegean coast of Turkey: *Posidonia oceanica* (L.) Delile meadows. *Journal of the Black Sea/Mediterranean Environment* 18 (3).
- Erkanal, H., 2008. Liman Tepe: new light on prehistoric aegean cultures. In: Erkanal, H., Hauptmann, H., Şahoglu, V. (Eds.), *The Aegean in the Neolithic, Chalcolithic and the Early Bronze Age*. Proceedings of the International Symposium, Urla-Izmir, pp. 179–190.
- Erkanal, H., 2017. Liman Tepe Kazıları. *Kazı Sonuçları Toplantısı*, pp. 387–406.
- Flatman, J.C., Evans, A.M., 2014. Prehistoric archaeology on the continental shelf: the state of the science in 2013. In: Evans, A.M., Flatman, J., Flemming, N. (Eds.), *Prehistoric Archaeology on the Continental Shelf*. Springer, USA, pp. 1–12.
- Fleming, K., Johnston, P., Zwart, D., Yokoyama, Y., Lambeck, K., Chappell, J., 1998. Refining the eustatic sea-level curve since the Last Glacial Maximum using far- and intermediate-field sites. *Earth Planet Sci. Lett.* 163 (1–4), 327–342.
- Flemming, N.C., 2020. Global experience in locating submerged prehistoric sites and their relevance to research on the American continental shelves. *J. I. Coast Archaeol.* 1–24.
- Flemming, N.C., Harff, J., Moura, D., Burgess, A., Bailey, G.N. (Eds.), 2017. *Submerged Landscapes of the European Continental Shelf: Quaternary Paleoenvironments*, vol. 1. John Wiley & Sons.
- Giaime, M., Marriner, N., Morang, C., 2019. *Earth Sci. Rev.* 191, 141–167.
- Göktaş, F., 2016. Neogene stratigraphy of the Izmir outer-bay islands. *Bulletin of the Mineral Research and Exploration* 152 (152), 1–24.
- Goodman, B.N., 2006. *The Paleogeography of Liman Tepe, Turkey: A Multi-Proxy Geoarchaeological Study*. McMaster University. Unpublished PhD thesis.
- Goodman, B.N., Reinhardt, E.G., Dey, H.W., Boyce, J.I., Schwarcz, H.P., Şahoglu, V., Erkanal, H., Artzy, M., 2008. Evidence for Holocene marine transgression and shoreline progradation due to barrier development in Işkele, Bay of Izmir, Turkey. *J. Coast Res.* 24 (5), 1269–1280.
- Goodman, B.N., Reinhardt, E.G., Dey, H.W., Boyce, J.I., Schwarcz, H.P., Şahoglu, V., Erkanal, H., Artzy, M., 2009. Multi-proxy geoarchaeological study redefines understanding of the paleocoastlines and ancient harbours of Liman Tepe (Işkele, Turkey). *Terra. Nova* 21 (2), 97–104.
- Gregory, B.R., Patterson, R.T., Reinhardt, E.G., Galloway, J.M., Roe, H.M., 2019. An evaluation of methodologies for calibrating Itrax X-ray fluorescence counts with ICP-MS concentration data for discrete sediment samples. *Chem. Geol.* 521, 12–27.
- Harff, J., Bailey, G.N., Lüth, F., 2016. Geology and archaeology: submerged landscapes of the continental shelf: an introduction. *Geological Society, London, Special Publications* 411 (1), 1–8.
- Heaton, T.J., Köhler, P., Butzin, M., Bard, E., Reimer, R.W., Austin, W.E.N., Bronk Ramsey, C., Hughen, K.A., Kromer, B., Reimer, P.J., Adkins, J., Burke, A., Cook, M.S., Olsen, J., Skinner, L.C., 2020. Marine20—the marine radiocarbon age calibration curve (0–55,000 cal BP). *Radiocarbon* 62 (4), 779–820.
- Heisserer, A.J., 1980. *Alexander the Great and the Greeks*. University of Oklahoma Press, Norman, Oklahoma.
- Ingram, W.C., Meyers, S.R., Brunner, C.A., Martens, C.S., 2010. Late Pleistocene–Holocene sedimentation surrounding an active seafloor gas-hydrate and cold-seep field on the Northern Gulf of Mexico slope. *Mar. Geol.* 278 (1–4), 45–53.
- Jolivet, L., Faccenna, C., Huet, B., Labrousse, L., Le Pourhiet, L., Lacombe, O., Lecomte, E., Burrov, E., Denèle, Y., Brun, J.P., Philippon, M., Paul, A., Salaün, G., Karabulut, H., Piromallo, C., Monié, P., Gueydan, F., Okay, A., Oberhänsli, R., Pourteau, A., Augier, R., Gadenne, L., Triussi, O., 2013. Aegean tectonics: strain localisation, slab tearing and trench retreat. *Tectonophysics* 597, 1–33.
- Kaya, O., 1979. Ortadoğu ege çöküntüsünün (neojen) stratigrafisine tektoniği. *Turk.*

- Jeol. Kurumu Bul. 22 (1), 35–58.
- Kayan, İ., 1988. Late Holocene sea-level changes on the western Anatolian coast. *Palaeogeogr. Palaeoclimatol. Palaeoecol.* 68 (2–4), 205–218.
- Kayan, İ., Öner, E., Doğan, M., İlhan, R., Vardar, S., 2019. Holocene paleogeography and geoarchaeological interpretations on the Urla-İskele coastal plain. *Aegean Geographical Journal* 28 (1), 11–32.
- Kayan, İ., 2019. Holocene sea level changes and their geoarchaeological impacts on the Aegean coast of Anatolia. *TINA Maritime Archaeology Periodical* 12, 11–35.
- Koparal, E., Ersoy, Y.E., Massa, M., Demirciler, C., 2018. Sampling the ionian landscapes: an overview of the archaeological surveys in the klazomenian and teian chorai. In: Steadman, S.R., McMahon, G. (Eds.), *The Archaeology of Anatolia Volume II: Recent Discoveries (2015–2016)*. Cambridge Scholars Publishing, p. 407.
- Koster, B., Vött, A., Mathes-Schmidt, M., Reicherter, K., 2015. Geoscientific investigations in search of tsunami deposits in the environs of the agoulinitsa peatland, kaiafas lagoon and kakovatos (gulf of kyparissia, western peloponnese, Greece). *Z. Geomorphol.* 59, 125–156.
- Krezoski, G., 2008. *Paleoenvironmental Reconstruction of Prehistoric Submerged Shorelines and Coastal Environments at Liman Tepe-Klazomenai, Turkey*. Unpublished Master's thesis, McMaster University, p. 139.
- Lambeck, K., 1995. Late Pleistocene and Holocene sea-level change in Greece and south-western Turkey: a separation of eustatic, isostatic and tectonic contributions. *Geophysics Journal International* 122 (3), 1022–1044.
- Lambeck, K., Rouby, H., Purcell, A., Sun, Y., Sambridge, M., 2014. sea level and global ice volumes from the last glacial maximum to the Holocene. *Proc. Natl. Acad. Sci. Unit. States Am.* 111 (43), 15296–15303.
- Lök, A., Açarlı, S., 2006. Preliminary settlement studies of flat oyster (*Ostrea edulis*, L.) on oyster and mussel shell collectors in Karantina Island (Turkey). *Isr. J. Aquac. Bamiidgeh* 58 (2), 105–115.
- Löwemark, L., Chen, H.F., Yang, T.N., Kylander, M., Yu, E.F., Hsu, Y.W., Lee, T.Q., Song, S.R., Jarvis, S., 2011. Normalizing XRF-scanner data: a cautionary note on the interpretation of high-resolution records from organic-rich lakes. *J. Asian Earth Sci.* 40 (6), 1250–1256.
- Mellet, C.L., Plater, A.J., 2018. Drowned barriers as archives of coastal response to sea-level rise. In: Moore, L.J., Murray, A.B. (Eds.), *Barrier Dynamics and Response to Changing Climate*. Springer, pp. 57–89.
- Micallef, A., Fogliini, F., Le Bas, T., Angeletti, L., Maselli, V., Pasuto, A., Taviani, M., 2013. The submerged paleolandscape of the Maltese Islands: morphology, evolution and relation to Quaternary environmental change. *Mar. Geol.* 335, 129–147.
- Missiaen, T., Sakellariou, D., Flemming, N.C., 2017. Survey strategies and techniques in underwater geoarchaeological research: an overview with emphasis on prehistoric sites. In: Bailey, G., Harff, J., Sakellariou, D. (Eds.), *Under the Sea: Archaeology and Palaeolandscapes of the Continental Shelf*, vol. 20. Coastal Research Library, Springer, Cham, pp. 151–164.
- Morhange, C., Pirazzoli, P.A., Evelpidou, N., Marriner, N., 2012. Late Holocene tectonic uplift and the silting up of Lechaion, the western harbor of ancient Corinth, Greece. *Geoarchaeology* 27 (3), 278–283.
- Morton, R.A., White, W.A., 1997. Characteristics of and corrections for core shortening in unconsolidated sediments. *J. Coast Res.* 761–769.
- Müller, C., Woelz, S., Ersoy, Y., Boyce, J., Jokisch, T., Wendt, G., Rabbel, W., 2009. Ultra-high-resolution marine 2D–3D seismic investigation of the Liman Tepe/Karantina Island archaeological site (Urla/Turkey). *J. Appl. Geophys.* 68 (1), 124–134.
- Paul, M.A., Barras, B.F., 1998. A geotechnical correction for post-depositional sediment compression: examples from the Forth valley, Scotland. *J. Quat. Sci.: Published for the Quaternary Research Association* 13 (2), 171–176.
- Pint, A., Seeliger, M., Frenzel, P., Feuser, S., Erkul, E., Berndt, C., Klein, C., Pirson, F., Brückner, H., 2015. The environs of Elaia's ancient open harbour—a reconstruction based on microfossil evidence. *J. Archaeol. Sci.* 54, 340–355.
- Piva, A., Asioli, A., Schneider, R.R., Trincardi, F., Andersen, N., Colmenero-Hidalgo, E., Dennielou, B., Flores, J.-A., Vigliotti, L., 2008. Climatic cycles as expressed in sediments of the PROMESS1 borehole PRAD1-2, central Adriatic, for the last 370 ka: 1. Integrated stratigraphy. *G-cubed* 9 (1).
- Rampino, M.R., Sanders, J.E., 1980. Holocene transgression in south-central long island, New York. *J. Sediment. Res.* 50 (4), 1063–1079.
- Reimer, P.J., Austin, W.E., Bard, E., Bayliss, A., Blackwell, P.G., Ramsey, C.B., Butzin, M., Cheng, H., Edwards, R.L., Friedrich, M., Grootes, P.M., 2020. The IntCal20 Northern Hemisphere radiocarbon age calibration curve (0–55 cal kBP). *Radiocarbon* 62 (4), 725–757.
- Reynolds, D.J., Steckler, M.S., Coakley, B.J., 1991. The role of the sediment load in sequence stratigraphy: the influence of flexural isostasy and compaction. *J. Geophys. Res.: Solid Earth* 96 (B4), 6931–6949.
- Riddick, N.L., 2021. *Coastal Palaeoenvironmental Change and Ancient Harbour Development at Liman Tepe-Clazomenae (Urla, Turkey) and Lechaion (Corinth, Greece): A Multi-Proxy Geoarchaeological and Geophysical Study*. McMaster University. Unpublished PhD thesis.
- Riddick, N.L., Boyce, J.I., Reinhardt, E.G., Rothaus, R.M., Chomiccki, K.M., McCarthy, F.M., 2021a. Multi-proxy palaeoenvironmental record of coastal tectonic uplift and abandonment (ca. 6th c. CE) of Lechaion's inner harbour, ancient Corinth, Greece. *Quat. Sci. Rev.* 267, 107080.
- Riddick, N.L., Boyce, J.I., Krezoski, G.M., Şahoğlu, V., Erkanal, H., Tuğcu, I., Alkan, Y., Gabriel, J.J., Reinhardt, E.G., Goodman-Tchernov, B.N., 2021b. Datasets: Palaeoshoreline reconstruction and underwater archaeological potential of Liman Tepe: a long-occupied coastal prehistoric settlement in western Anatolia, Turkey. Mendeley Data. <https://data.mendeley.com/datasets/hm9x276fj/1>.
- Riddick, N.L., Boyce, J.I., Şahoğlu, V., Erkanal, H., Tuğcu, I., Yeşim, A., Reinhardt, E.G., and Goodman-Tchernov, B.N., in review. Coastal palaeoenvironmental record of Late Bronze to Iron Age harbour development at Clazomenae-Liman Tepe, western Anatolia, Turkey. *Marine Geology*.
- Rothaus, R.M., Reinhardt, E.G., Noller, J.S., 2008. Earthquakes and subsidence at Kenchreai: using recent earthquakes to reconsider the archaeological and literary evidence. In: Caraher, W.R., Hall, L.J., Moore, R.S. (Eds.), *Archaeology and History in Roman, Medieval and Post-medieval Greece: Studies on Method and Meaning in Honor of Timothy E. Gregory*. Ashgate Publishing Ltd., pp. 53–66.
- Rothwell, R.G., Croudace, I.W., 2015. Micro-XRF studies of sediment cores: a perspective on capability and application in the environmental sciences. In: Croudace, I.W., Rothwell, R.G. (Eds.), *Micro-XRF Studies of Sediment Cores*. Springer, pp. 1–24.
- Şahoğlu, V., 2005. The Anatolian trade network and the Izmir region during the early Bronze age. *Oxf. J. Archaeol.* 24 (4), 339–361.
- Sakellariou, D., Galanidou, N., 2017. Aegean Pleistocene landscapes above and below sea-level: palaeogeographic reconstruction and hominin dispersals. In: Bailey, G.N., Harff, J., Sakellariou, D. (Eds.), *Under the Sea: Archaeology and Palaeolandscapes of the Continental Shelf*. Springer, pp. 335–359.
- Sayın, E., 2003. Physical features of the Izmir bay. *Continental Shelf Res.* 23 (10), 957–970.
- Sayın, E., Eronat, C., 2018. The dynamics of İzmir Bay under the effects of wind and thermohaline forces. *Ocean Sci.* 14 (2), 285–292.
- Scott, D.B., Hermelin, J.O.R., 1993. A device for precision splitting of micropaleontological samples in liquid suspension. *J. Paleontol.* 67 (1), 151–154.
- Sonnenburg, E.P., Boyce, J.I., 2008. Data-fused digital bathymetry and side-scan sonar as a base for archaeological inventory of submerged landscapes in the Rideau Canal, Ontario, Canada. *Geoarchaeology* 23 (5), 654–674.
- Sonnenburg, E.P., Boyce, J.I., Suttak, P., 2012. Holocene palaeoshorelines, water levels and submerged prehistoric site potential of Rice Lake (Ontario, Canada). *J. Archaeol. Sci.* 39 (12), 3553–3567.
- Stiros, S.C., 2020. Coastal subsidence, destruction layers and earthquakes from an underwater archaeological excavation: Kenchreai, eastern harbour of Roman Corinth, Greece. *Mediterranean Geoscience Reviews* 1–15.
- Stuiver, M., Reimer, P.J., Reimer, R.W., 2021. CALIB 8.2 [WWW program] at. <http://calib.org>.
- Tan, O., Tapırdamaz, M.C., Yörük, A., 2008. The earthquake catalogues for Turkey. *Turk. J. Earth Sci.* 17 (2), 405–418.
- Tartaron, T.F., 2013. *Maritime Networks in the Mycenaean World*. Cambridge University Press.
- Tartaron, T.F., Pullen, D.J., Dunn, R.K., Tzortzopoulou-Gregory, L., Dill, A., Boyce, J.I., 2011. The Saronic harbors archaeological research project (SHARP): investigations at Mycenaean Kalamianos, 2007–2009. *Hesperia* 80 (4), 559–634.
- Taymaz, T., Yilmaz, Y., Dilek, Y., 2007. The geodynamics of the Aegean and Anatolia: introduction. *Geological Society, London, Special Publications* 291 (1), 1–16.
- Tjallingii, R., Statterger, K., Wetzel, A., Van Phach, P., 2010. Infilling and flooding of the Mekong River incised valley during deglacial sea-level rise. *Quat. Sci. Rev.* 29 (11–12), 1432–1444.
- Tuncel, R., Şahoğlu, V., 2018. The chalcolithic of coastal western Anatolia: a view from liman tepe, Izmir. In: Dietz, S., Mavridis, F., Tabkocis, Z., Takaoglu, T. (Eds.), *Communities in Transition: the Circum-Aegean Area during the 5th and 4th Millennia BC*. Oxbow Books Limited.
- Vacchi, M., Rovere, A., Chatzipetros, A., Zouros, N., Firpo, M., 2014. An updated database of Holocene relative sea level changes in NE Aegean Sea. *Quat. Int.* 328, 301–310.
- Votruba, G.F., Artzy, M., Erkanal, H., 2016. A set Archaic anchor arm exposed within P. oceanica mat at Klazomenai/Liman Tepe, Turkey: a contribution for understanding marine stratigraphy. *J. Field Archaeol.* 41 (6), 671–683.
- Vousdoukas, M.I., Velegakis, A.F., Plomaritis, T.A., 2007. Beachrock occurrence, characteristics, formation mechanisms and impacts. *Earth Sci. Rev.* 85 (1–2), 23–46.
- Westley, K., Plets, R., Quinn, R., 2014. Holocene paleo-geographic reconstructions of the Ramore Head area, Northern Ireland, using geophysical and geotechnical data: paleo-landscape mapping and archaeological implications. *Geoarchaeology* 29 (6), 411–430.